UCSF
UC San Francisco Electronic Theses and Dissertations

**Title**
Elucidating cellular mechanisms of mosaicism and identifying potential drug treatments in Fibrous Dysplasia

**Permalink**
https://escholarship.org/uc/item/8b03s1qq

**Author**
Lung, Hsuan

**Publication Date**
2020

Peer reviewed|Thesis/dissertation

eScholarship.org Powered by the California Digital Library
University of California

# Elucidating cellular mechanisms of mosaicism and identifying potential drug treatments in Fibrous Dysplasia

by
Hsuan Lung

DISSERTATION
Submitted in partial satisfaction of the requirements for degree of
DOCTOR OF PHILOSOPHY

in

Oral and Craniofacial Sciences

in the

GRADUATE DIVISION
of the
UNIVERSITY OF CALIFORNIA, SAN FRANCISCO

Approved:

DocuSigned by:
Tamara Alliston
E233CABEF261499...

Tamara Alliston
Chair

DocuSigned by:
Edward Hsiao
DocuSigned by:
Ralph Marcucio
DocuSigned by:
Marina Sirota
925B61AB9C41499...

Edward Hsiao
Ralph Marcucio
Marina Sirota

Committee Members

Copyright (2020)

by

Hsuan Lung

**ACKNOWLEDGEMENTS**

Edward Hsiao, MD, PhD

Tamara Alliston, PhD
Ralph Marcucio, PhD
Marina Sirota, PhD

Robert Nissenson, PhD
Chelsea Bahney, PhD

Sunita Ho, MS, PhD
Misun Kang, PhD

Kelly Wentworth, MD
Tania Moody

Hsiao Lab present and past members

Pamela Den Besten, DDS, MS
Roger Mraz

An Nguyen
Nick Chang, MS
Erin Malone

OCS program faculty and students

## CONTRIBUTIONS

The text of Chapter 1 of this dissertation is a reprint of the manuscript as it appears in Frontiers of Endocrinology. The co-authors listed in this publication directed and supervised the research that forms the basis for the dissertation.

Lung, H., E.C. Hsiao, and K.L. Wentworth, *Advances in Models of Fibrous Dysplasia/McCune-Albright Syndrome.* Front Endocrinol, (Lausanne) 2019. **10**: p. 925.

## ABSTRACT

Elucidating cellular mechanisms of mosaicism and identifying potential drug treatments in Fibrous Dysplasia

by

Hsuan Lung, DDS

**Background:**

G protein-coupled receptor (GPCR) signaling mediates a wide spectrum of physiological functions, including bone development and remodeling. Fibrous dysplasia (FD) is a common skeletal dysplasia where normal bone and bone marrow are replaced by fibrous tissue and expansile trabecular bone lesions. The craniofacial bones are often involved, leading to pain and facial deformities. FD is a mosaic disease caused by a somatic mutation in the *GNAS* gene encoding the G-protein alpha subunit ($G_s\alpha$) that leads to constitutive activation of the $G_s$ signaling pathway via increased cyclic AMP (cAMP) levels. Unfortunately, FD has no effective medical treatments.

Major challenges have hampered the development of pharmacologic strategies that specifically target *GNAS* or the $G_s\alpha$ protein. We previously developed the $ColI(2.3)^+/Rs1^+$ mouse model (Rs1) in which the $G_s$ signaling pathway is activated specifically in bone by an engineered GPCR protein. These mice showed increased trabecular bone formation

with loss of marrow space and cortical bone, which strongly resembles human FD. There was also a dramatic increase in the number of immature osteoblasts present in the FD lesions, suggesting that activation of $G_s$ signaling caused an accumulation of these cells. Our prior studies showed that the FD-like lesions had increased Wnt signaling, which may be a major driver of the phenotype. Furthermore, blocking the $G_s$ signaling could reverse the abnormal bone phenotype, providing proof-of-concept for finding drugs that could reverse the phenotype.

**Methods:**

Long bones from 2 wildtype and 2 ColI(2.3)$^+$/Rs1$^+$ 9-week-old male mice were used to isolate stromal cells for scRNAseq analyses. Differentially expressed genes between clusters and between experimental groups within clusters were ascertained using Seurat. The cell types in each cluster were identified using SingleR to match gene expression in each cluster to existing databases. To test the role of Wnt signaling, we performed global Wnt inhibition on the ColI(2.3)$^+$/Rs1$^+$mouse model using the porcupine inhibitor LGK974. The mice were evaluated by histology and micro computed tomography (micro-CT). Finally, drug repositioning analysis was performed by comparing the molecular disease signature of FD we created from our single cell gene expression

data. Our disease signature was queried against pharmacological agents in Broad Institute's Connectivity Map database (CMap).

**Results:**

The cellular compositions between WT control and ColI(2.3)$^{+}$/Rs1$^{+}$ bones as identified from our scRNAseq data were similar, except that there was a significant increase in the total number of cells with an expansion of osteoblastic lineage cells. The osteoblast cluster also had the highest number of differential expression (DE) genes. Expression of $G_i$ coupled receptors were increased, potentially as a compensatory mechanism for the strong activation of $G_s$-GPCR pathway induced by Rs1 expression. In addition, the scRNAseq data revealed activation of the GH/IGF1 signaling pathway in osteoblastic cells in the FD-like bone lesions. The scRNAseq data also identified broad expression of many Wnt ligands within the bone cells, including within the osteoblast cluster. Treatment with the broad Wnt production inhibitor of porcupine, LGK974, showed resorption of the abnormal FD bone; however, the fibrocellular infiltrate in the ColI(2.3)$^{+}$/Rs1$^{+}$ mice was still present. Drugs from the Connectivity Map database that have opposite gene expression patterns to FD were identified through our computational analysis and are candidates for testing as potential treatment of FD.

**Conclusions:**

This study uses a translational approach combining a unique mouse model of FD to elucidate the cellular interactions in FD-like lesions and create a novel gene expression disease signature of FD. We found that broad Wnt inhibition can lead to decreased fibrous dysplastic bone, but the fibrocellular infiltrate does not appear to fully reverse. These results provide new insight into understanding interactions between the Wnt and $G_s$ signaling pathways in FD pathogenesis and bone formation. Together, this work expands our understanding of FD pathogenesis and helps identify potential strategies for treatment, laying a strong foundation for future research on GPCR signaling and bone development.

**Keywords:**

Fibrous dysplasia (FD), *Gnas*, $G_s\alpha$, scRNAseq, Wnt inhibition, drug repositioning

**TABLE OF CONTENTS**

## LIST OF FIGURES

## LIST OF TABLES

## CHAPTER 1: INTRODUCTION

Musculoskeletal disorders such as skeletal dysplasias are a significant health problem affecting both children and adults. Bone formation is tightly controlled for when and where it happens - but when this tight regulation is perturbed - it can cause abnormal bone formation, leading to a number of pathological conditions for which there are gaps in clinical care.

A variety of cellular pathways, including G-protein coupled receptors (GPCRs) and their ligands, have been identified as key regulators of osteoblast formation and function – two critical steps in normal bone formation and homeostasis. The human GPCR family includes over 340 non–olfactory and 400 olfactory receptors [1], making it the largest class of receptors in the human genome. GPCRs mediate a wide variety of biological processes and are activated by multiple types of extracellular signals, ranging from photons and ions to small molecules to peptides. The diversity of GPCRs and their responses to small molecules has made them major targets for over 40% of modern pharmaceuticals [2].

GPCRs signal through a select number of canonical pathways [3]: among these, the $G_s$ and $G_i$ pathways increase or decrease intracellular cAMP levels, respectively,

by acting on adenylate cyclase, while the $G_q$ pathway increases intracellular calcium by activating phospholipase C.

McCune-Albright Syndrome (MAS) is a proto-typical disease caused by activating mutations in the *GNAS* locus, encoding the $G_s\alpha$ protein [4]. MAS is a mosaic genetic disease characterized by the classic triad of polyostotic fibrous dysplasia (FD) of the bone, café-au-lait skin hyperpigmentation, and peripheral precocious puberty. Patients with MAS may have other endocrinopathies, including Cushing's syndrome, hyperthyroidism, acromegaly, and solid organ malignancies of the breast, thyroid, and pancreas. FD/MAS is caused by an acquired somatic mutation in *GNAS*, the gene that encodes the alpha subunit of the stimulatory G-protein ($G_s\alpha$), leading to constitutive activation of $G_s\alpha$ signaling in affected cells. This mutation occurs post-zygotically, resulting in tissue mosaicism, and is not inherited through the germline. As a result of this mosaicism, the clinical disease spectrum of FD ranges from single bone involvement to multi-organ involvement. The most common cause is a missense mutation at either position c.602G>A (p.R201H) or c.601C>T (p.R201C). This mutation results in an amino acid substitution in the GTP hydrolase domain of the $G_s\alpha$ protein, inhibiting the intrinsic GTPase activity, and leading to persistently elevated intracellular cAMP levels.

**Clinical Presentation of Fibrous Dysplasia**

A major clinical feature of MAS is FD of the bone, where expansile bone lesions cause fragility, malformations, and pain (Figure 1.1). FD also occurs without MAS, and is a common congenital skeletal dysplasia that can affect one bone (mono-ostotic) or multiple bones (polyostotic) [5, 6]. FD is arguably the most significant medical complication of MAS, since no effective treatments are available to manage the bone complications. In addition, the broad clinical spectrum of FD/MAS and the mosaic nature of the disease leads to variability in the radiographic presentation, sometimes making FD challenging to accurately diagnose.

In 2019, the FD/MAS International Consortium put forth a position statement to help guide clinicians in the diagnosis and management of FD/MAS [6]. The first step in diagnosing FD/MAS is to perform a complete skeletal and extra-skeletal evaluation to determine the extent of the disease. MAS can be diagnosed if a patient has FD and at least one extraskeletal manifestation (café-au-lait skin hyperpigmentation, peripheral precocious puberty, thyroid lesions consistent with FD/MAS, growth hormone excess, and neonatal hypercortisolism*)* or the absence of skeletal involvement but 2 extra-skeletal manifestations [6]. An accurate diagnosis of FD/MAS can usually be made after a complete physical examination, combined with biochemical, hormonal, and

radiologic evaluation of the skeletal, dermatologic, and endocrine systems. Biopsy of FD lesions is needed only if there is uncertainty about the diagnosis (i.e., atypical radiologic features) or concern for underlying malignancy [6]. In these situations, affected tissue can be tested for the presence of a *GNAS* activating mutation, with the understanding that false negatives may occur if the sample has a low mutational burden. Peripheral blood is usually not sufficient for diagnosis due to the mosaicism of the disease. Next-generation sequencing is associated with a lower false-positive rate [6].

**Treatment and Monitoring of FD/MAS**

Comprehensive guidelines regarding the management of the skeletal and extra-skeletal manifestations of FD/MAS were recently published, and should be considered when caring for patients along this clinical disease spectrum [6]. The mainstay of therapy in FD/MAS remains adequate pain control, optimization of phosphate and vitamin D status, treatment of IGF-1 excess if present, and judicious consideration of surgical resection of FD lesions once they have stabilized. Unfortunately, there are no effective medical treatments available for FD/MAS. Bisphosphonate therapy in IV formulation has been reported to provide some benefits for pain control in patients with persistent moderate-to-severe pain from FD lesions, but why this helps in only some patients

remains unclear [7-9]. In addition, there is no evidence to suggest that bisphosphonates decrease the progression of FD lesions, and may not adequately control pain in some patients [9, 10].

Presently, there is minimal evidence for the use of denosumab (RANKL inhibitor) and other anti-resorptive agents in FD, although there are case reports suggesting potential clinical benefits [7]. However, there are major concerns about rebound fractures and FD lesion progression after drug cessation [7]. Ongoing clinical trials to address the utility of denosumab in FD are underway (NCT03571191). In addition, the TOCIDYS trial is evaluating the efficacy of IL-6 inhibition in patients with FD who did not have improvement in pain with prior bisphosphonate treatment (NCT01791842*).* These exciting trials hold promise for identifying potential medical strategies for mitigating the complications from FD. However, a better molecular understanding of FD and the pathways involved in the progression of FD lesions is needed to better fill the current gap in clinical care.

**Mouse Models for Understanding FD**

One contributor to the dearth of effective treatments for FD/MAS is the complexity of the *GNAS* locus. This complexity has made it challenging to develop robust mouse and

human models to dissect the mechanisms of FD/MAS. During the past several years, several novel strategies for uncovering the roles of $G_s$-GPCR signaling in bone have been developed. These models provide critical insights into the pathogenesis and potential therapeutic approaches for FD.

One of the earliest models utilized the PTH/PTH-related protein (PTH/PTHrP) receptor (PPR), a GPCR, to study Jansen's metaphyseal chondrodysplasia (JMC). JMC is a rare form of short-limbed dwarfism caused by activating mutations of the PPR, leading to constitutive receptor activation and ligand-independent intracellular cAMP accumulation. Calvi et al generated a mouse (Col1-caPPR) that expressed the human mutant PPR HKrk-H223R (caPPR), one of the causative mutations associated with JMC, in osteoblastic lineage cells in mice using a Col1α1 (2.3kB) promoter [11]. At 1 week of age, these mice showed increased osteoblast number and function in both the trabecular bone and the endosteal surface of cortical bone in the long bones. However, periosteal osteoblast activity was inhibited. This resulted in an increase in trabecular bone volume and a decrease in cortical bone thickness in the long bones. Calvarial thickness remained unchanged but there was increased porosity and bone remodeling on the endosteal surface of the skull. There was also an increased number of mature osteoclasts in these mice, which led to increased porosity of the cortical bone. At 2

weeks of age, excess bone formed in the bone marrow space [12]. The area between the trabeculae was occupied by fibrous cells, blood vessels, and osteoclasts. There was delayed formation of bone marrow cavities, adipocytes, and hematopoietic cells. Surprisingly, these dysplastic bone and fibrous tissue phenotypes gradually resolved over time, and were limited to the metaphyseal area at 4 months. These studies showed that when the constitutively active PPR was expressed in osteoblastic lineage cells, the receptor could mediate both the anabolic and resorptive effects of PTH, and that PPR is involved in the regulation of both bone marrow and stromal tissues.

Our group used a different approach, creating an engineered GPCR RASSL (receptor activated solely by a synthetic ligand) to regulate GPCR signaling [13]. The $G_s$-coupled receptor, Rs1, was created by inserting a D100A mutation into the wild-type human 5HT4 serotonin receptor [14]. This engineered receptor has a high basal level of constitutively active $G_s\alpha$ activity and is not responsive to the endogenous serotonin ligand. The $ColI(2.3)^+/Rs1^+$ mouse model (Figure 1.2) limits Rs1 expression spatially to osteoblastic lineage cells by using a Col1α1(2.3kb) promotor, and temporally using the tet-off system, which allows for controlled expression of Rs1 in the absence of doxycycline. The FD-like phenotype of mice born off doxycycline was first apparent at 6 days [15]. These mice showed age-dependent, increased trabecular bone formation with

loss of marrow space and thinned cortical bone. The histologic and radiographic features strongly resemble human FD of the bone. There was also a dramatic increase in the number of immature osteoblasts present in the FD lesions, deposition of immature bone tissue, and reduced mineralization seen in analyses by FTIR spectroscopy and synchrotron radiation micro-computed tomography [16]. Rs1 mice also showed lower numbers of hematopoietic stem cells[17]. ColI(2.3)$^{+}$/Rs1$^{+}$ mouse bones also showed dramatically reduced mature adipocyte differentiation, and higher osteoblastic glucose utilization than control mice[18]. RNA analysis on whole bone samples showed increased Wnt signaling, suggesting that Wnt proteins may be a major driver of this effect [18]. Importantly, blocking $G_s$ signaling by using doxycycline at 4 weeks gradually reversed the bone phenotype [15], providing a proof-of-concept that therapies inhibiting $G_s$ signaling may be effective for reversing fibrous dysplastic bone lesions. This model provides a powerful tool for understanding the effects of $G_s$-GPCR signaling on dynamic bone growth and remodeling.

In contrast to strategies that did not directly manipulate *GNAS*, Saggio et al generated a transgenic mouse model of human FD that constitutively expressed *GNAS*-R201C [19]. The transgene expression did not show any appreciable effect on embryonic skeletal formation and unlike human FD, could be vertically transmitted. FD

lesions were detected radiographically at 6 months of age. The lesions first appeared in the tail and later progressed to the femurs and the skull. The onset and progression of lesions were defined in three stages: an early phase (<2 months), defined by abnormal trabecular bone formation, endosteal thickening, and ectopic cortical lesions; an intermediate phase (2 to 6 months), with narrowed marrow cavity, expanded cortical bone and increased osteoclastic activity; and a late phase (>10 months) described as the fibrous dysplastic phase, with abnormal bone trabeculae and matrix fibrous tissue. At one year of age, the skeletal features resembled human FD.

When *GNAS*-R201C expression was limited to maturing osteoblasts using the Col1α1 (2.3kb) promoter, changes in bone structure were detected on radiograph at 3 weeks in the tail, with excess bone mass [20]. At 3 months, increased bone density was noted in all bones. The transgenic mice showed excess bone formation and remodeling of the bone marrow space. However, the expression using the Col1α1(2.3kb) promoter failed to reproduce other features of human FD, such as bone marrow space fibrosis, and the loss of adipocytes and hematopoietic cells seen in other models [19, 21].

Palmisano et al tested the effect of RANKL (receptor activator of nuclear factor kappa-B ligand) inhibition by treating the mice with an anti-RANKL antibody [22]. They found that new and highly mineralized bone replaced the FD-like lesions in 2-month old

mice, and the bone density increased radiographically. The treatment also stopped the growth of pre-existing FD lesions. In addition, there was a higher maximum load and stiffness of the bones in the treated group. However, the FD-like lesions progressed after RANKL inhibitor cessation.

More recently, Zhao et al developed a mouse model expressing *GNAS*-R201C in the skeletal stem cell lineage using a tetracycline-inducible Cre-mediated Prrx1 driver transgene [23]. The FD bone phenotype was observed in embryos and adult mice less than 2 weeks after doxycycline administration (to activate the transgene) at E4.5. The FD lesions in the long bones showed reduced endochondral ossification, and in craniofacial bones showed decreased mineralization in the calvarial sutures. Poorly mineralized trabeculae and a dense fibrous matrix were present, and the bone marrow spaces were also decreased. When doxycycline was administered to 3-week old mice for 2 weeks (to induce expression), all limbs developed FD-like lesions with expansive bone deformities, fractures in limb bones, and defects in calvarial sutures. Doxycycline withdrawal resulted in reversal of the bone lesions. Hematopoietic cells and adipocytes appeared in the bone marrow of former FD lesions. The skulls of the reversed *GNAS*-R201C mice also showed normal morphology with closed sutures.

Finally, Khan et al generated a new conditional knock-in mouse model [*GNAS*f(R201H)] using a minigene cassette to express human *GNAS*-R201H at the endogenous mouse *GNAS* locus [24]. They found that expression of *GNAS*-R201H in the germ-line using Sox2-Cre resulted in embryonic lethality. Using Prrx1-Cre, they limited the expression of *GNAS*-R201H to osteochondral progenitor cells and early limb bud mesenchyme cells. At P0, control mice had well-formed cortical bone, cartilaginous epiphyses, and a normal marrow cavity. In contrast, Prrx1-Cre; *GNAS*f(R201H)/+ showed no bone formation. At P6, Prrx1-Cre; *GNAS*f(R201H)/+ mice showed bone formation, but the marrow space was replaced by fibrous tissue and trabecular bone. In mutant long bones, higher levels of Wnt/β-catenin were also noted. At 3 weeks of age, there was more FD bone formation in the Prrx1-Cre; *GNAS*f(R201H)/+ mice; expansion of woven trabecular bone; lack of cortical bone; and increased osteoclasts. Furthermore, in this mouse model, Xu et al demonstrated that $G_s\alpha$ signaling mediated intramembranous ossification of cranial bones by regulating both Hh and Wnt/β-catenin signaling [25].

Together, these mouse models demonstrate that FD bone lesions can develop from activating mutations at the $G_s$-GPCR level as well as from transgenic expression or knock-in expression of a *GNAS* allele carrying the R201C or R201H activating mutation.

In addition, data from several mouse models suggest that blocking $G_s$ pathway hyperactivity can lead to reversal of the FD bone lesions and may be a viable treatment strategy for human FD.

**Human Cellular Models of $G_s$-signaling**

Human cellular models have contributed significantly to our understanding of FD/MAS pathophysiology, and patient-derived tissue samples have been an invaluable source. In 1998, Bianco et al performed one of the earliest studies using FD/MAS patient bone marrow samples and showed that bone marrow stromal cell (BMSC) progenitors isolated from fibrous dysplastic lesions were either heterozygous for the $G_s\alpha$ activating mutant allele, or homozygous wildtype. This discovery demonstrated that the skeletal progenitor cell population in FD lesions is mosaic, with a resident population of bone marrow stromal cells harboring the mutation and another population that is unaffected [26]. When these cells were transplanted into immunocompromised mice, the wildtype colonies developed normal ossicles, but the colonies containing the *GNAS* mutant allele only did not survive and did not form ossicles. However, when a mixture of wildtype and mutant cell colonies was transplanted, an abnormal ossicle formed, with histopathologic features resembling FD. These experiments provided strong evidence that both wildtype

and mutant cells were necessary to form a FD lesion, and that the mosaicism inherent to FD/MAS can be recapitulated within an FD lesion [26].

This novel concept of somatic mosaicism within an FD lesion was explored further by Kuznetsov et al [27]. In their study, they isolated colony forming unit-fibroblasts (CFU-Fs) from FD lesions of patients with FD/MAS and calculated the frequency of mutation-bearing CFU-Fs versus normal CFU-Fs. They noted an inverse relationship between patient age and the number of mutated skeletal stem cell colonies present within an FD lesion, and concluded that the number of mutated stem cells must undergo apoptosis as patients age. Similarly, the bone histology in older patients (32-52 years of age) with FD/MAS was less severe than that of younger patients, and was more likely to be associated with a lower *GNAS* mutational burden. They hypothesized that as skeletal stem cells aged, there may be preferential apoptosis of mutated cells, resulting in loss of these cells and self-renewal of non-mutated cell populations. This could account for the decreased incidence of new FD lesions and the relative stability of existing FD lesions as patients age. Kuznetsov et al also transplanted cell colonies containing CFU-Fs into immunocompromised mice and showed that FD ossicles formed, whereas non-mutant CFU-Fs or mutation-positive strains without mutant skeletal stem cell populations did not

form FD ossicles. Thus, they concluded that *GNAS* mutations within the skeletal stem cell population was sufficient to induce formation of FD lesions [27].

Piersanti et al developed a model in which human skeletal progenitor cells were engineered to stably over-express the *GNAS*-R201C mutation using a lentiviral vector [28].These cells demonstrated elevated cAMP production, consistent with over-expression of $G_s$. When cultured *in vitro,* they did not exhibit mineralization and had lower osteocalcin levels than controls. Levels of the osteogenic markers alkaline phosphatase and bone sialoprotein were elevated compared to controls, and the cells exhibited robust RANKL expression, consistent with the profound osteoclastogenesis seen in most human FD lesions. Additionally, genes in the phosphodiesterase pathway were upregulated in these cells, suggesting an adaptive response to $G_s$ over-expression. When these cells were transplanted into immunocompromised mice, the stably-transduced *GNAS*-R201C cells formed ossicles but were unable to differentiate into adipocytes or hematopoietic components. Finally, silencing of the *GNAS*-R201C allele with lentiviral vectors containing short hairpin interfering RNA sequences caused these cells to revert to their normal state and no longer exhibit a mutant phenotype.

In 2019, de Castro et al used human FD-derived BMSCs from a well-characterized cohort of FD patients at the NIH to show that RANKL expression in FD skeletal lesions

may directly contribute to osteoclast induction in FD lesions [29]. They showed that serum levels of RANKL were 16-fold higher in FD patients compared with healthy controls, and the serum RANKL/OPG ratio was 12-fold higher. The magnitude of increase in RANKL and RANKL/OPG was positively correlated with total body skeletal disease burden score, a well-validated scoring system used to determine the severity of FD.

de Castro et al also isolated BMSCs from FD patients and healthy volunteers and showed that RANKL levels were higher in the conditioned media of FD BMSCs compared with BMSCs derived from healthy volunteers when stimulated with prostaglandin E2 (PGE2) and 1,25 vitamin D3 [29]. These cells also released OPG, but to a much lower degree than healthy volunteer controls. Additionally, when FD BMSCs were co-cultured in osteogenic media with peripheral monocytes from healthy volunteers, the monocytes differentiated into TRAP+ osteoclasts; however, when cultured in non-osteogenic media, they did not induce osteoclastogenesis. They subsequently showed that osteoclastogenesis could be inhibited when the cell co-cultures were treated with denosumab. This study provided strong evidence that RANKL is expressed in human FD lesions and is correlated with disease burden, thus

implicating RANKL over-expression as an important contributor to FD pathogenesis and informing the design of ongoing studies testing denosumab in FD (NCT03571191).

**Wnt Signaling in Bone**

Our prior work and that of other groups have shown that changes in $G_s$-GPCR signaling can dramatically affect the bone niche, including hematopoietic stem cell function [17, 30, 31], fracture repair [32, 33], and osteogenic cell fate [34, 35]. This appears to occur through both direct GPCR signaling and activation of ancillary pathways such as Wnt [24, 36], Hedgehog [37], and Yap/Taz [38]. Expression of the activating GNAS R201H allele using a PRRX1-cre could induce a cranial bone phenotype, that could be reversed by blocking Wnt signaling activity. However, whether Wnt blockade can affect established FD-like bone lesions in the setting of continued activated $G_s\alpha$ activity remains unknown.

The Wingless (Wnt) pathway is a major regulator of many developmental processes, including that of bone and cartilage development [39]. Wnt ligands stimulate osteoblast proliferation and support osteoblast maturation. Wnt signaling plays a critical role in postnatal osteogenic differentiation of mesenchymal stem cells [40], and is a key regulator of the balance between osteogenesis and adipogenesis [41].

A study [42] investigating the interactions between $G_s\alpha$ and Wnt/β-catenin signaling in FD found increased Wnt/β-catenin signaling in FD bone tissues. However, Wnt/β-catenin signaling and bone formation were decreased after removing $G_s\alpha$. The activating mutant $G_s\alpha$ protein in osteoprogenitor cells up-regulated Wnt/β-catenin signaling and inhibited osteoblast maturation, producing the FD phenotype. Upon reduction of Wnt/β-catenin signaling, the defect in maturation was rescued. Furthermore, the four major Gα proteins ($G_s\alpha$, $G_i\alpha/o$, $G_q\alpha/11$, and $G_{12/13}\alpha$) differentially regulated the Wnt/β-catenin signaling, where $G_s\alpha$ led to increased Wnt/β-catenin signaling. However, the Gα proteins were not required for Wnt/β-catenin signaling. The Wnt pathway is a focus of this disssertation research and will be discussed in more detail in Chapter 2.

**Drug repositioning and computational approaches to identify potential drugs for Fibrous Dysplasia**

Drug repositioning is the application of approved drugs to new therapeutic indications and offers several advantages over traditional drug development including reduced development costs and shorter paths to approval. Recent approaches to drug repositioning use high-throughput approaches to assess a compound's potential

therapeutic qualities [43, 44].

**Conclusions and Areas of Research Needs**

The past 15 years have shown major advances in our understanding of FD/MAS. There are striking consistencies among the mouse models of FD, and a number of features of the human disease are replicated in the mouse genetic models, suggesting that direct targeting of the $G_s$ pathway has strong potential as a therapeutic strategy for FD. In addition, the human cell models of FD are providing new tools for understanding FD pathogenesis and cell-type specific effects of the *GNAS* activating mutations. Finally, international collaborations among clinicians and researchers with strong experience in FD/MAS are yielding best-practice recommendations and treatment guidelines for optimal management of FD/MAS.

Despite these advances, there remain several fundamental questions about FD that need to be answered in order to develop effective therapies. First, the specific cell types that express Wnt or other drivers of FD bone lesions remains unknown. Second, the exact role of the Wnt pathway in FD pathogenesis remains unknown, including whether inhibition of Wnt is sufficient to block or reverse existing FD bone lesions. Finally, although our prior data shows that inhibiting the $G_s$ signaling pathway can reverse FD

bone lesions, whether existing drugs can be utilized for this purpose (via drug repositioning) remains unknown.

Here, we use a combination of single-cell RNA sequencing (scRNAseq) and global Wnt inhibition on the ColI(2.3)$^{+}$/Rs1$^{+}$ mouse model that develops a strong FD-like bone phenotype to better understand the roles of $G_s$-GPCR pathway activation and Wnt in driving the trabecular bone formation process. By identifying the gene profile of cells with activated $G_s$ signaling in FD and using a drug repositioning approach, we may discover pharmaceutical agents that could reverse the FD gene expression changes.

## CHAPTER 2: Global Wnt Inhibition with a Porcupine Inhibitor Decreases Established Trabecular Bone in a Mouse Model of Fibrous Dysplasia

### INTRODUCTION

The Wingless (Wnt) pathway is a major regulator of many developmental processes, including that of bone and cartilage development [39]. Wnt ligands stimulate osteoblast proliferation and support osteoblast maturation. Wnt signaling plays a critical role in postnatal osteogenic differentiation of mesenchymal stem cells [40], and is a key regulator of the balance between osteogenesis and adipogenesis [41].

The three major Wnt signaling pathways that have been characterized are the canonical Wnt/β-catenin pathway, the non-canonical planar cell polarity (PCP) pathway, and the non-canonical Wnt/calcium pathway [45]. The canonical pathway signals through the β-catenin protein, and is a major regulator of skeletal tissue regeneration and repair[46]. In the planar cell polarity (PCP) pathway, Wnt signaling activates the Jun N-terminal kinase (JNK) and regulates cytoskeletal control of cell shape and cell polarity (Geetha-Loganathan et al., 2008). The Wnt/calcium pathway activates phospholipase C (PLC), protein kinase C (PKC), and calmodulin-dependent kinase II, and regulates calcium inside the cell (Kestler and Kuhl, 2008). Wnt ligands are encoded by 19 Wnt genes. This diversity reflects their wide and varied role in

development and tissue homeostasis. The ligands bind receptors on the cell surface of recipient cells to activate the Wnt pathway (Willert and Nusse 2012). The Wnts that have been found to signal via the canonical pathway are Wnt1, 2, 2b, 3, 3a, 8a, 8b, 10a, 10b [47]; and by the non-canonical pathway are Wnt4, 5b, 6, 7a, 7b, 11. Wnt5a has been found to be involved in both canonical and non-canonical pathways [48]. All of the Wnts are processed by the acyltransferase porcupine by palmitoylation in the endoplasmic reticulum of Wnt-producing cells [49]. Porcupine is required for optimal secretion of all Wnt ligands.

For many years, the GNAS activating mutations were thought to cause FD bone lesions solely by increasing cAMP production and activating downstream cAMP signaling pathways. However, patients with Carney's syndrome, caused by activating mutations in the regulatory unit of PRKAR1A, show hyperpigmented skin lesions and bony abnormalities that are different from McCune-Albright Syndrome. This suggested that *GNAS* might activate other pathways distinct from cAMP that could impact bone formation and the FD/MAS phenotype.

More recently, data suggests that the Wnt and GNAS pathways can interact with each other. A study [42] investigating the interactions between $G_s\alpha$ and Wnt/β-catenin signaling in FD has found increased Wnt/β-catenin signaling in FD bone tissues.

However, Wnt/β-catenin signaling and bone formation were decreased after removing $G_s\alpha$. The activating mutant $G_s\alpha$ protein in osteopregenitor cells up-regulated Wnt/β-catenin signaling and inhibited osteoblast maturation, producing the FD phenotype. Upon reduction of Wnt/β-catenin signaling, the defect in maturation was rescued. Furthermore, the four major Ga proteins ($G_s\alpha$, $G_i\alpha/o$, $G_{q/11}\alpha$, and $G_{12/13}\alpha$) differentially regulated the Wnt/β-catenin signaling, where $G_s\alpha$ led to increased Wnt/β-catenin signaling. However, the Gα proteins were not required for Wnt/β-catenin signaling.

These results indicate that the Wnt pathway likely has a major role in driving the formation of FD like bone in mice. However, the spectrum of Wnt ligands produced; the cells that produce these ligands; and whether direct inhibition of Wnt ligand production could reverse existing FD, are all questions that remained unknown. This project set out to examine these fundamental questions.

FD is thought to require tissue mosaicism to develop a disease phenotype [26]. The specific identities of the cells that have increased $G_s$ activation are unclear. FD bone lesions contain many cell types, including the highly prolific fibrous cells characteristic of the lesions. In addition, there is a very large expansion in the number of immature osteoblastic cells by histology. Single cell RNA sequencing (scRNAseq) has the potential

to identify genes in the Wnt/β-catenin pathway that are altered by $G_s$ signaling and cell populations in the bone that express Wnt. We have used single cell sequencing techniques to distinguish different cell populations and elucidate the cell autonomous and non-autonomous pathways in FD.

## MATERIALS AND METHODS

### ColI(2.3)$^{+}$/Rs1$^{+}$ mouse model of FD-like bone lesions

ColI(2.3)$^{+}$/Rs1$^{+}$ mice were maintained on the FVB/N background and were generated by heterozygote crosses of mice carrying the TetO-Rs1 transgene (MMRRC 030758) with mice carrying the Col1(2.3)-tTA transgene (MMRRC 029992) [21]. The Rs1 transgene is an engineered G-protein coupled receptor based on the human serontonin 5HT4b receptor, and results in a receptor with high constitutive $G_s$-GPCR signaling activity. We previously showed that these mice develop a strong, dramatic bone phenotype characterized by high trabecular bone formation and fibrocellular infiltrates, which strongly resembled human FD bone lesions, when maintained on regular chow (LabDiet 5053, PMI Nutrition) to allow continuous activation of the Rs1 transgene from gestation, as previously described [21]. All mouse studies were approved by the Institutional Animal Care and Use Committee and the Laboratory Animal Research Center at the University of California, San Francisco.

### Tissue collection and single-cell RNA sequencing (scRNAseq)

We collected long bones (hip, femur, tibia, fibula, humerus, radius, and ulnar bones) from 2 wildtype and 2 ColI(2.3)$^{+}$/Rs1$^{+}$ 9-week-old male mice (Figure 2.1.1A). Bones were

gently crushed using mortar and pestle using a previously published osteoblast isolation protocol [17]. The bone fragments were washed with PBS to separate the hematopoietic cells from the bone chips, which contain the osteoblastic lineages of interest. Bone chips were incubated in collagenase type I (Worthington) suspended in PBS without FBS for 60 minutes at 37℃ on an orbital shaker at 110 RPM. Collagenase was neutralized by adding 5ml FBS [Seradigm] and then centrifuged at 1200 rpm for 5 minutes, then resuspended in 2 ml of 2%FBS in PBS. Isolated stromal cells were passed over a dead cell removal procedure by using magnetic activated cell sorting (MACS) (Miltenyi Biotec,130-090-101) using the manufacturer's instructions. scRNAseq libraries were generated by the UCSF Genomics Core using the 10X Genomics Chromium Single Cell 3′ Kit v.2 according to the manufacturer's protocols, and sequenced on an Illumina NovaSeq. The raw sequencing data was processed using Cell Ranger version 2.2.0 (10X Genomics) using a modified 10X mouse transcriptome mm10-1.2.0 as a reference. The 10X prebuilt reference package does not contain sequences for the Rs1 transgene so we used the CellRanger mkref command to modify the mm10 reference. A FASTA file containing sequences for the Rs1 receptor and the tTA fragment was created along with an annotation or GTF file for these sequences. The files were added to the existing mm10 reference to create our custom reference. In the downstream analysis, we used

the read counts from the tTA transgene instead of Rs1 since Rs1 (human HTR4 mutation) is too similar to other serotonin receptors to be uniquely identifiable by scRNAseq, and therefore may pose an issue with multi-mapping.

**scRNAseq data preprocessing**

Gene expression matrices produced by CellRanger for each mouse sample were processed by SoupX (v1.4.5) to remove ambient RNA contamination [50]. Subsequent quality control steps were performed using Seurat (v3.2.2) [51, 52]. Low quality cells were removed from sample datasets by removing cells with fewer than 200 expressed genes. Genes expressed in fewer than 3 cells were also removed. Approximately half the cells in each of the samples were red blood cells (RBCs). The majority of RBCs were filtered out by removing cells with greater than 100 Hba-a1 gene transcripts. Low quality cells identified as having greater than 5% mitochondrial genes in the transcriptome were removed. Probable doublets were removed by filtering out cells with greater than 5500 genes. Cells with genes above this number were outliers with respect to the per cell gene number as were cells with less than 600 genes (presumed dead cells), which were also removed. SingleR (v1.0.1) was used to identify any remaining RBCs [52]. Cells identified by SingleR as 'Erythrocytes' were removed. The two WT and two ColI(2.3)$^{+}$/Rs1$^{+}$

samples contained 7974, 6874, 7463, and 6484 cells, respectively, prior to filtering, After filtering, 3441, 2326, 3562, and 2070 WT and Coll(2.3)$^{+}$/Rs1$^{+}$ cells were retained for downstream analysis for a total of 11,399 cells.

Gene expression data for each cell was normalized using the “LogNormalize” method where counts for each cell are divided by the total expression, multiplied by a scale factor of 10,000, and then natural-log transformed using log1p. The 2000 most highly variable genes in each sample were identified using Seurat’s ‘vst’ method implementation in preparation for downstream analyses [51, 52].

**scRNAseq data analysis**

Integration of data and clustering of cells was performed in Seurat according to guidelines provided by the Sajita Lab [51, 52]. Briefly, after integration of datasets, expression data for the most highly variable features was scaled so that the mean expression across cells is 0. Variables representing the percent of mitochondrial RNA, the percent of ribosomal RNA, and the total number of RNA reads were regressed out against the scaled data. Linear dimensional reduction of the scaled data was performed using PCA. Clusters were identified using K-nearest neighbor graphing and the Louvain algorithm. Uniform Manifold Approximation and Projection (UMAP) dimensional

reduction technique was used to visualize the clusters. Differentially expressed (DE) genes between clusters and between experimental groups within clusters were ascertained using a Wilcoxon Rank Sum test. SingleR (v1.0.1), which leverages reference transcriptomic datasets (ImmGen and Mouse-RNAseq) of pure cell types to infer each cell's origin, was used to annotate cluster cell types [53]. To complement SingleR's cell type annotations, we performed literature searches of top DE genes in each cluster, checked known cell type marker expression in the clusters, and submitted select expression matrices to the Mouse Cell Altas for annotation (not shown) [54].

Biological and functional pathways were identified using Enrichr [55] and Ingenuity Pathway Analysis (IPA) [Qiagen Inc., [56]]. Monocle [57] was used for pseudotime analysis to identify potential developmental relationships.

**Pharmacologic inhibition of Wnt signaling**

Four-week old ColI(2.3)$^{+}$/Rs1$^{+}$ mice were treated with the porcupine (PCN) inhibitor LGK974 (Millipore (CAS 1243244-14-5)) to inhibit Wnt pathway activity. The LGK974 was resuspended in a mixture of DMSO (5ug LGK974/100ul DMSO), then dissolved in corn oil to achieve final doses of 5mg/kg/50ul or 30mg/kg/50ul. LGK974 was administered by oral gavage with either a low dose (5mg/kg) for 8 weeks or high dose

(30mg/kg) for 4 weeks, starting at 4 weeks of age and for 5 days each week. Both male and female mice were used in this study. Control animals were either single transgenic or wildtype littermates, as prior studies indicated no significant differences among these control genotypes [21]. Mice receiving no LGK974 received only corn oil vehicle by gavage.

**Bone imaging**

Gross changes in bone mass were assessed by dual energy x-ray absorptiometry (DEXA, GE Lunar Piximus2) at baseline and at 4 (high-dose groups) or 12 (low-dose groups) weeks of age following prior protocols [21]. Whole-body areal bone mineral density (BMD) and bone mineral content (BMC) were measured, excluding the head. Standard microCT was performed on formalin fixed femurs at the indicated time points. Specimens were imaged at 5μm resolution on a MicroCT50, Scanco Medical, Switzerland) at Core Center for Musculoskeletal Biology and Medicine (CCMBM), UCSF. We analyzed 100 slices of the mid- diaphysis at 5um for both cortical and trabecular parameters [21] For high resolution microCT, we used a MicroXCT-200 (Carl Zeiss Microscopy, Pleasanton, CA, USA) at the UCSF Biomaterials and Bioengineering Correlative Microscopy Core. Specimens were imaged at 10X magnification (spatial

resolution: ~2μm/voxel) and 60kVp of energy. Tomograms were reconstructed after beam hardening, center shift correction, and CT scaling using XMReconstructor. The same subvolume (~0.6$mm^3$) of each sample was extracted and segmented in order to determine bone mineral density ($mg/cm^3$), bone volume ($mm^3$), trabecular thickness (μm), and connectivity with AVIZO software (Thermo Fisher Scientific Inc., Hillsboro OR, USA). Bone mineral density was measured based on the calibration curve obtained using known mineral density calibration phantoms (detailed calibration protocol in [58]. Bone volume ($mm^3$), trabecular thickness (μm), and connectivity were determined by the materials statistics, thickness map, and auto skeleton modules, respectively.

**Histology**

Femur bones were collected in 10% neutral buffered formalin for 24 hours followed by decalcification in 10% ethylenediaminetetraacetic acid (EDTA, pH 7.4). EDTA was changed 5 times per week until bones were pliable. WT bones were decalcified for 1 week and $Coll(2.3)^+/Rs1^+$ bones for 3 weeks. Bones were processed by the Gladstone Light and Microscopy Core (San Francisco) by embedding in paraffin, longitudinal sectioning at 5 microns thickness, and staining with hematoxylin and eosin (H&E).

**Immunohistochemistry**

Formalin fixed decalcified bones were embedded in paraffin and sectioned longitudinally at 5 um. After deparaffinization, endogenous peroxidase was blocked with 3% $H_2O_2$ for 30 minutes at room temperature (RT) and non-specific blocking with 2% goat serum for 20 minutes at RT. Bones were assessed by immunohistochemistry for numbers of immature and mature osteoblasts, and osteoclasts using the primary antibodies osterix (Sp7, Abcam, #ab22552, 1:1000), osteocalcin (OC, Takara, #M173, 1:1000), and Cathepsin K (Abcam, #ab19027, 1:250) respectively. Primary antibodies diluted in PBST/1%BSA and negative control were applied to the sections overnight at 4°C. Then secondary antibody (Amersham NA9340V, 1:250) was diluted in PBST/1%BSA and applied for 45 minutes at RT. Positive staining was detected using the DAB (3,3'-diaminobenzidine) Substrate Kit for Peroxidase (Vector, Cat# SK-4100) according to manufacturer's protocol and counterstaining was performed with hemotoxylin (Mayer, Sigma, 51275) for 15 seconds.

**Statistical analysis**

Differences between the control and experimental groups were calculated using an unpaired 2-tailed *t* test (GraphPad Prism and Microsoft Excel). Analyses were

considered statistically significant if $p$ <0 .05.

The Generalized Estimating Equation-I (GEE-I) [59] was used to deal with repeated measurements and to determine the associated factor of four genotypes (Col1, WT, Rs1, ColI(2.3)$^{+}$/Rs1$^{+}$ (mut)) with treatment response and bone mineral density (BMD) in total of 27 mice. The analyzed variables including sex, weight, times, groups (with or without drug), four genotype of Col1, WT, Rs1 and ColI(2.3)$^{+}$/Rs1$^{+}$ (mut), and BMD ((ROI) g/cm$^{3}$) were all brought into GEE-I analysis.

We anticipated that the BMD would increase with time (ß=-0.018, p<0.001), because the mice would grow up with time. Four different genotypes, Col1, WT, Rs1, and ColI(2.3)$^{+}$/Rs1$^{+}$ (mut), were used to explore the BMD toward drug treatment during four weeks. The GEE-I analysis resulted, only the mut genotype had a statistically significantly increasing in the BMD after four weeks (ß=0.029, p<0.001). There were no differences in BMD between sex and group, consistent with our prior findings.

## RESULTS

### ColI(2.3)+/Rs1+ mice show increased numbers of osteoblastic cells, but not other lineages.

FD of the bone is histologically characterized by a fibrocellular infiltrate accompanied by the prolific formation of fine trabecular bone [60]. However, the specific identities of these cells and their molecular characterization has been elusive. Our prior studies [21] and those in other mouse models of $G_s$ overactivation [11, 19, 23, 24] suggest that these fibrocellular cells represent a large expansion of the osteoblastic lineage. To better understand the spectrum of cells present in a FD-like bone lesion, we performed scRNAseq on the stromal cell portion of our ColI(2.3)$^+$/Rs1$^+$ mice.

Major non-cranial bones were harvested from the ColI(2.3)$^+$/Rs1$^+$ mice and crushed to extract cells [17]. The CD45$^-$ cells were single cell sequenced (Figure 2.1.1A) from two control and two ColI(2.3)$^+$/Rs1$^+$ mice. Each sample captured 6000-8000 cells (Table 2.2). A total of 28,733 cells were captured in all 4 samples together. After applying quality control measures to remove doublets and apparent dead cells, a total of 11,809 cells were analyzed (Table 2.2). The mean reads per cell ranged from 49934-84283 reads, and the median genes per cell ranged from 798-1027 genes. These measures were in line with the expected yields and QC measures.

The individual cells were first filtered and clustered (Table 2.1) using Seurat [61, 62], and then compared together. We identified 11 distinct clusters based on gene expression (clusters 0-10) (Figure 2.1.1.B). Comparison of the cell clusters isolated from control and $ColI(2.3)^{+}/Rs1^{+}$ mice showed a major difference in absolute cell numbers and frequency only within cluster 8 (Table 2.2). In addition, the number of differentially expressed genes was highest in cluster 8, which included the osteoblasts (903 genes), while the other clusters showed significantly fewer differentially expressed genes (range 6-337 genes).

The cell types in each cluster were identified using SingleR to match gene expression in each cluster to existing databases [53] (Figure 2.1.1.C). Cell types of fibroblast-like cell (including osteoblasts), granulocytes, monocytes, B cells, NK cells, and ethryoblasts were easily identified. We then used known markers of granulocytes, monocytes, B cells, NK cells and ethryocytes, combined with SingleR, to further divide the different hematopoietic cell types (Figure 2.1.2). No major differences in the populations of erythrocytes, B cells, monocytes, NK cells, graulocytes, or granulocyte-monocyte progenitors were evident (Table 2.3).

Osteoblasts [53] were further identified using established markers for osteoblastic lineage cells [Sp7 (osterix), Col1α1 (collagen 1α1), and Bglap2 (osteocalcin)]. These genes were strongly expressed in cluster 8 (Figure 2.1.1.D). Expression of Col1α1 were

higher in the ColI(2.3)$^{+}$/Rs1$^{+}$ cells. These results also showed that the number of Runx2-expressing precursor cells were similar between WT and ColI(2.3)$^{+}$/Rs1$^{+}$ bones, and that the largest expansion of cells in ColI(2.3)$^{+}$/Rs1$^{+}$ bones expressed Col1α1 and Sox9. Although the Runx2 precursors are unchanged, there was a favoring of ColI(2.3)$^{+}$/Rs1$^{+}$ cells transitioning into more specific osteoblastic lineages, as indicated by Col1α1 and Bglap. Unexpectedly, Sox9 expression was also increased in ColI(2.3)$^{+}$/Rs1$^{+}$ cells, as Sox9 is a marker of the cartilage lineage [63].

**Pathway analyses with IPA identify potential roles for Wnt and Igf1 pathways.**

Cluster 8 was further sub-clustered into clusters 8a and 8b (Figure 2.2.1.A). ColI(2.3)$^{+}$/Rs1$^{+}$ cells were spread out in clusters 8a and 8b while WT cells were mostly in cluster 8a. Col1α1 was higher expressed in cluster 8b and Col9α1 in 8a. Pathway analyses of ColI(2.3)$^{+}$/Rs1$^{+}$ (Mut) vs. WT osteoblasts (cluster 8) using genes with a differential expression p value of <0.05 (903 genes within the threshold) (Figure 2.2.1B) was performed using Ingenuity Pathway Analysis (IPA) [56]. Due to the low number of differentially expressed genes and low representation of genes in each pathway, traditional pathway analyses using gene frequency approaches were not possible. The

low number of differentially expressed genes decreased our sensitivity to identify altered pathways; however, we could assess representative genes involved in several key pathways known to be activated by GNAS signaling including Wnt, Hedgehog, Hippo, and the $G_s/G_i/G_q$ G protein signaling pathways[25, 42].

Ingenuity Pathway Analysis on cluster 8 (Figures 2.2.1.C, 2.2.2) was able to identify changes in the Wnt/β-catenin signaling pathway, including down regulation of Wnt4 and Wnt5b were decreased in Coll(2.3)$^+$/Rs1$^+$ cells, while Wnt2 and Wnt9a were up-regulated in Coll(2.3)$^+$/Rs1$^+$ cells. Sox5, Sox6, Sox8, and Sox9 were down-regulated in the Coll(2.3)$^+$/Rs1$^+$ cells. Lrp1, c-Jun, Sfrp1, and CD44 were highly up-regulated in the Coll(2.3)$^+$/Rs1$^+$ cells. Surprisingly, the Wnt/β-catenin pathway in the whole bone sample was decreased, while Wnt/calcium and PCP pathway activities were increased. However, when looking at cluster 8 (osteoblastic cells) alone, the Wnt/β-catenin and PCP pathways were increased, and the Wnt/calcium pathway decreased, indicating that the osteoblastic cell population with activated $G_s$ signaling increases both canonical and PCP pathway Wnt activity. The sonic hedgehog signaling pathway was increased in the whole stromal cell sample, however, it was decreased in cluster 8.

Coll(2.3)$^+$/Rs1$^+$ cells showed increased levels of Igf1 (Insulin-like growth factor I) and other Igf binding proteins, which interacted with various genes. Igf1 is a mediator of

the effects of growth hormone, and growth hormone activity is thought to be a major driver of FD progression, especially McCune-Albright Syndrome patients [64]. The Igf1 signaling pathway is increased in ColI(2.3)$^{+}$/Rs1$^{+}$ cells in cluster 8 (Figure 2.2.3). Igf1 is more highly expressed (logFC) in ColI(2.3)$^{+}$/Rs1$^{+}$ cells and the percentage of cells that express Igf1 is larger. Although the level of expression of Jun is increased, the number of cells that express Jun is similar to WT cells.

We also looked at the differentially-expressed genes of GPCR in IPA (Figure 2.2.4). 17 genes were differentially-expressed, and 8 genes were higher in ColI(2.3)$^{+}$/Rs1$^{+}$ cells. The log fold change (logFC) were highest in Lpar1 (Lysophosphatidic Acid Receptor 1) and F2r (Coagulation factor II receptor). The Pth1r and Fzd9 expressions were decreased in ColI(2.3)$^{+}$/Rs1$^{+}$ cells. In IPA analyses, the cAMP pathway was increased, which was expected in this constitutively active $G_s\alpha$ system. However, the $G_s\alpha$ signaling pathway was decreased, likely driven by inclusion of the Pthr1 gene in this IPA pathway. We also noted that the $G_i$ pathway was increased, which may serve as a compensatory mechanism.

**Wnt expression is elevated in the osteoblast cluster and other clusters.**

Activated $G_s$ signaling increases RNA expression of Wnt proteins (39), and inhibition of Wnt in the PRRx1-cre/GNASR201H mouse model could reverse a developmental phenotype in the skull. Prior studies on FACS-purified ColI(2.3)$^+$/Rs1$^+$ cultured cranial osteoblasts, using a ColI(2.3)-eGFP marker, showed no major differences in cell autonomous Wnt production as assessed by microarray [65]. To understand this difference, we examined our scRNAseq data for expression of Wnt proteins. As expected tTA expression (the driver for our Rs1 transgene) showed highest expression in the osteoblast cluster (cluster 8, Figure 2.1D). Of the known Wnt ligands (Figure 2.2.1D-E), Wnt6, 10a, 10b, 1, 2, 9a, and 16 were up-regulated. Wnt6 and Wnt10a are known regulators of osteoblast formation and function [41, 66]. Notably, expression of Wnt ligands were found in cluster 8, including Wnt1, 2, 4, 5a, 5b, 6, 9a, 10a, 10b, 11, and 16 (11 genes). The osteoblast cluster (cluster 8) showed high cell-autonomous expression of several Wnt proteins (Wnt2, Wnt9a) in the ColI(2.3)$^+$/Rs1$^+$ mice, compared to controls. Wnt expression was elevated in several other clusters that did not express tTA, including Wnt10a in cluster 4 (B cells), Wnt10b in cluster 6 (monocytes); and to a lesser degree Wnt4 in cluster 6 (monocytes). The osteoblast (OB) cluster (cluster 8) as

well as other cell clusters such as monocytes and B cells, expressed increased levels of Wnt6, Wnt10a, and Wnt10b, consistent with prior data [18]. We also found that Wnt1, Wnt2, Wnt9a, and Wnt16 were only expressed in the ColI(2.3)$^{+}$/Rs1$^{+}$ cells, and expressed across multiple clusters with expressions highest in the osteoblast cluster (cluster 8). These findings suggested that both cell and non-cell autonomous mechanisms are induced by $G_{s\alpha}$ overactivity to change Wnt expression.

**Monocle single-cell trajectory analysis shows three branching trajectories in the osteoblast cluster.**

Subclustering of the osteoblast cluster using Monocle trajectory analysis identified a developmental branch into the red (1), green (2), and blue (3) branches (Figure 2.2.1.F). Although the number of WT cells was limited, WT cells were found in the red and blue branches, suggesting that these states are found in normal bone structures. The green cluster is interesting as it contains only ColI(2.3)$^{+}$/Rs1$^{+}$ cells. This green cluster corresponds to cluster 8b, which had highest expression of Col1α1. Igf1 and Col1α1 are expressed in branch 2 (green). In branch 2 (green), where only consists of ColI(2.3)$^{+}$/Rs1$^{+}$ cells, Wnt2 and Wnt4 are involved in both β-catenin and planar cell polarity (PCP) pathways. The dot plot shows Wnt ligand gene expression in each branch.

Although cluster 8 was marked as the osteoblastic cells, by using Monocle to look at the cellular relationships, cluster 8 could be further sub-divided into 3 branches of cells which expressed different Wnt ligands.

**Low-dose treatment of Wnt inhibitor LKG974 shows slight thinning of established fibrous dysplastic trabecular bone.**

Because of the broad expression of multiple Wnt proteins identified by our scRNAseq data, we used the porcupine inhibitor LGK974 was used to test if generalized inhibition of Wnt production affected the formation of FD-like lesions. LGK974 [67] inhibits Wnt signaling by targeting porcupine, a Wnt-specific acyltransferase. It is currently in clinical trials of patients with malignancies involving the Wnt ligands (ClinicalTrials.gov ID NCT01351103).

4-week-old ColI(2.3)$^{+}$/Rs1$^{+}$ and littermate control mice were treated with LGK974 at 5mg/kg/day for 8 weeks *via* oral gavage (Figure 2.3.A). No major changes in the morphology on the H&E staining and CT scans between vehicle and LGK974 groups were identified, except for a subtle histological thickening of the trabecular bones in ColI(2.3)$^{+}$/Rs1$^{+}$ mice receiving LGK974 when compared to ColI(2.3)$^{+}$/Rs1$^{+}$ vehicle-treated group (Figure 2.3.B-E). The VOX-BV/TV, trabecular thickness, trabecular

separation showed no significant differences (Figure 2.3.F-G), but there was a significant increase of trabecular number in the ColI(2.3)$^{+}$/Rs1$^{+}$ with drug group. Notably, after 8 weeks of drug administration, the variability of CT measures significantly decreased in the drug-treated group.

**High-dose treatment of Wnt inhibitor LKG974 shows significant thinning of established fibrous dysplastic trabecular bone, replaced with fibrosis tissue.**

To assess if the response to LGK974 was dose dependent, an increased dose of 30 mg/kg/day [68] was administered to the mice. 3.5-5-week-old mutant and non-mutant mouse femurs (Figure 2.4.1.A) showed significant changes of the trabecular bone thickness on H&E staining (Figure 2.4.1.B, E.). Although the spacing density of the trabeculae decreased, histology showed that despite the decrease in FD bone, the FD cellular infiltrate was still present. Furthermore, fibrous material was still present.

3D reconstruction of the microCT scans of the non-mutant mice with LGK974 administration showed thinning of the cortical bone (Figure 2.4.1.C, F). This is reflected on the CT measures, with a significant decrease of VOX-BV/TV in the LGK974 treated group (Figure 2.4.1.D, G.). On the microCT slice images of mutant femurs, the BV/TV ratio and trabecular bone thickness decreased significantly. The micro-CT showed

significantly decreased trabecular bone thickness (p=0.0364, n=3) in the drug-treated group (22±2μm) compared with controls (17±2μm). However, there was no significant difference in mineral density. Histology showed resorption of the abnormal bone; however, the fibrocellular infiltrate in the Rs1 mice was still present.

Although the mice received treatment for 3.5-5 weeks, we did not see reappearance of the bone marrow space. Bone trabecular volume decrease, appearance of the bone marrow space, and a more defined cortical bone were seen in our previous studies [15, 21] after suppressing the Rs1 expression for 16 weeks. The treatment may need to be longer to see a more dramatic effect; however, the potential toxicity of the Wnt inhibitor may be limiting.

Coll(2.3)$^{+}$/Rs1$^{+}$ mice treated with LGK974 still showed persistent expression of Osterix (Sp7), Osteocalcin, and Cathepsin K (Figure 2.4.1.H-J). Cells positive for Osterix and Cathepsin K staining were found along the bone surface. The matrix was osteocalcin positive. These results show that the Wnt inhibitor LGK974 at high dose did not completely obliviate osteoblastic cells. The number of positive cells were not quantitatively different with LGK974 treatment. As above, because high-dose LGK974 resulted in early lethality, mice were collected at 3.5-5 weeks of age to avoid effects at the end of their lifespan. Sub-analyses of mice at 3.5-4 and 4.5-5 weeks showed

significant decrease of BV/TV in the 4.5-5 weeks old group, but not in the 3.5-4 weeks old group (Figure 2.4.2.A.). This suggests that the longer duration of LGK974 administration resulted in an increased effect on trabecular bone resorption.

These results suggest that the effects of LGK974 treatment is dose- and time-dependent in Rs1 mice. The bone mineral density (BMD) was measured by DEXA at baseline and after 4 weeks of vehicle or drug (Figure 2.4.2.B). After 4 weeks, the BMD significantly decreased in the drug group of both the mutant and non-mutant mice. $Coll(2.3)^{+}/Rs1^{+}$ mice with four weeks drug treatment presented statistically significant decrease in BMD than mice not receiving drug treatment (ß=-0.a11, p=0.009). However, there were no differences in BMD between other genotypes whether with or without drug treatment.

Wnt inhibitor LGK974 decreased fibrous dysplastic trabecular bone volume and thickness, but the fibrous cell infiltrate was still present, suggesting there are two mechanisms driving the two phenotypes (Figure 2.5), abnormal bone formation and the fibrocellular infiltrate. The immature osteoblasts and osteoclast function were not decreased based on histologic comparison. Since blocking of the $G_s$ signal [15] causes reversion of both the abnormal bone and fibrocellular infiltrates, these results suggest that $G_s$ signaling is a driver of the fibrosis and that Wnt signaling is a driver of the

abnormal bone formation. These results provide new insight into understanding interactions between the Wnt and $G_s$ signaling pathways in FD pathogenesis and bone formation, and potential pharmacologic therapies.

## DISCUSSION

Fibrous dysplasia of the bone is a dramatic condition associated with prolific bone formation. Although activating mutations in *GNAS* is well known to cause FD, how these FD lesions form and how $G_s$-GPCR signaling links to other bone regulatory pathways in FD has remained a mystery. Both $G_s$ signaling and Wnt/β-catenin are important pathways in bone formation, and previous studies have investigated the interaction between $G_s$ signaling and the Wnt/β-catenin pathway [42]. While there are direct cell-autonomous effects of $G_s$ signaling on Wnt pathway activity, the spectrum of Wnts produced in cell autonomous and non-cell autonomous manners have not been elucidated. Furthermore, it was unclear whether Wnt blockade would be sufficient to reverse established FD-like bone lesions.

This study used scRNAseq on the ColI(2.3)$^+$/Rs1$^+$ FD-like bone lesions and found that the osteoblastic cell populations are the main affected cell type, and a unique subset of cells found only in ColI(2.3)$^+$/Rs1$^+$ mouse bones could be identified. In addition,

multiple Wnt ligands are clearly expressed in both cell autonomous and non-cell autonomous manners, indicating a complex regulatory system where $G_s$ activation in the osteoblastic population has implications for other surrounding cell types. Finally, broad blockade of Wnt signaling with a potent inhibitor of Porcupine [67] could partially reverse the FD-like lesions.

We and others had previously shown that $G_s$ signaling can activate the classical Wnt/β-catenin pathway in Coll(2.3)$^+$/Rs1$^+$ mice [18], and in mouse models that express a *GNAS*-R201H transgene or as a knockin [24]. Wnts are major regulators of bone formation and also regulate mesenchymal stem cell differentiation into adipocytes and cartilage. Although $G_s$ signaling can regulate the Wnt, Hh, and Yap/Taz pathways directly, FD has a curious requirement for tissue mosaicism to develop a disease phenotype [26]. Several hypotheses have been advanced, including a potential need for activated $G_s$-GPCR signaling in skeletal stem cell populations [24, 60]; however, activation of $G_s$ signaling in osteoblastic cells can also induce a FD-like bone lesion. The Coll(2.3)$^+$/Rs1$^+$ mouse model allows us to tag and identify cell populations that have the activated $G_s$-GPCR signaling, and elucidate how $G_s$ activation in those cells can lead to increased trabecular bone formation.

The scRNAseq data from the Coll(2.3)$^+$/Rs1$^+$ mice identified several unique features.

First, the cellular compositions between WT control and ColI(2.3)$^{+}$/Rs1$^{+}$ bones were surprisingly similar. Similar to prior studies, there is a significant increase in the total number of cells with an expansion of osteoblastic lineage cells [17], consistent with the large increase in bone mass in the ColI(2.3)$^{+}$/Rs1$^{+}$ mice. However, the cluster identified as osteoblasts within the stromal cell population that was sequenced showed the greatest difference in cell numbers/frequency, as well as differentially expressed genes, indicating that there is a strong cell autonomous effect induced by ColI(2.3) driven expression of Rs1. Surprisingly, this osteoblastic cluster could be sub-clustered to identify a cell population that appears to be unique to the ColI(2.3)$^{+}$/Rs1$^{+}$ mouse. Although we were unable to identify suitable cell surface markers to FACS purify these cells, we would speculate that this cell population is a major contributor to the cellular fibrosis characteristic of FD-like bone lesions, including that of ColI(2.3)$^{+}$/Rs1$^{+}$ mice. In addition, the osteoblastic cell cluster showed that not all cells expressed the tTA transgene, which we used as a marker of Rs1 expression. This is consistent with prior immunohistochemistry that had shown scattered Rs1 expression within ColI(2.3)$^{+}$/Rs1$^{+}$ lesions [21] and suggests that a non-cell autonomous effect, such as cAMP induced changes on neighboring cells [26], might be important for inducing changes in neighboring cells.

The scRNAseq data showed several intriguing findings related to GPCR expression in the ColI(2.3)$^{+}$/Rs1$^{+}$ FD like bone lesions. Multiple GPCRs are expressed in bone [69-74]. The parathyroid hormone (PTH) receptor (PTH1R) is the best studied in regards to bone formation and function. Polymorphisms in PTHR1, affecting the signaling properties of the receptor, are linked to variations in bone mineral density [75]. Mice expressing a constitutively active $G_s$–coupled PPR in osteoblasts show increased trabecular bone volume and decreased cortical bone thickness at 12 weeks of age, with grossly normal femur shape and size [11]. Superactivation of the $G_s$-GPCR pathway could also induce massive trabecular bone formation and effacement of cortical bone [19, 21, 23, 24]. Expression of $G_s$-GPCR receptors were significantly decreased in the osteoblastic cells, such as the Pth1r gene, but $G_i$ coupled receptors were increased, potentially as a compensatory mechanism for the strong activation of $G_s$-GPCR pathway induced by Rs1 expression. In addition, the scRNAseq data revealed activation of the GH/IGF1 signaling pathway in osteoblastic cells in the FD-like bone lesions. This is intriguing since growth hormone hyperactivity in McCune-Albright Syndrome is associated with promotion of FD bone lesion expansion in humans [6].

The scRNAseq data showed that there was broad expression of many Wnt ligands within the bone cells. The Wnt ligands (Wnt1, Wnt2, Wnt6, Wnt9a, Wnt10a, Wnt10b,

Wnt16) were found to be highly expressed in the osteoblast cluster, suggesting that there is direct activation of these Wnt pathways with $G_s$-GPCR activation. The Wnt/β-catenin pathway in the whole sample was decreased, while Wnt/calcium and PCP were increased. However, when looking at cluster 8 alone, the Wnt/β-catenin and PCP pathways were both increased, and the Wnt/calcium pathway decreased.

Previous qPCR expression analysis of whole bone had identified that Wn6, Wnt10a, and Wnt10b gene expression were increased in the $Col I(2.3)^+/Rs1^+$ bones, but that increased Wnt expression was not detectable in osteoblasts isolated by FACS gating method Schepers 2012 [17]. This discrepancy is now addressed by the scRNAseq data, as Wnt2 and Wnt9a were more highly expressed in a cell autonomous manner, with a parger proportion of cells expressing those genes. Surprisingly, a number of Wnt ligands were also produced by non-osteoblastic cells. While the specific mechanism that induces these changes remains unknown, the strongest induction appeared in Wnt2, Wnt9a, Wnt10a, and Wnt10b in osteoblasts, monocytes and B cells. Understanding how this non-cell autonomous effect occurs is an area of active investigation.

The broad and dramatic expression of Wnts by multiple cell types suggested that manipulation of individual Wnts may not be sufficient to block the FD-like bone formation in the $Col I(2.3)^+/Rs1^+$ mice. LGK974 is a broad inhibitor of Wnt ligand production and

targets the porcupine processing gene that enables secretion of all WNT ligands. LGK974 ~~is~~ in clinical trials on patients with cancer (ClinicalTrials.gov ID NCT01351103) and thus provided a way to test the role of Wnts within the Coll(2.3)$^{+}$/Rs1$^{+}$ bone lesions. Treatment with LGK974 could significantly reverse the active trabecularization that occurs in the setting of activated $G_s$-GPCR activity, but only at high doses that pushed tolerability. Although necropsies on mice receiving the highest dose of LGK974 did not reveal any obvious cause of death, the study of adverse events in the LGK974 clinical trial is still ongoing. Blocking the Wnt signaling significantly decreased the fibrosis that was present as assessed by histology, but the bone marrow space remained compromised after the short 4 week treatment course. These findings suggest that the Wnt ligands likely drive the fibrotic cell expansion seen in FD, and that the trabecular bone formation driven by those cells can be blocked by Wnt blockade.

There are several important limitations to our study. Although scRNAseq provides a powerful tool to assess gene expression in mosaic diseases, the low depth of sequencing, relatively low number of cells, low sensitivity due to the need to identify expressed genes from only the first 100 bp of sequence, and high expense for larger sample sizes, makes it very difficult to extrapolate comprehensive RNA expression data and differential expression analyses. This also limits the application of the scRNAseq

since identification of the GNAS-R201H mutation within the scRNAseq reads is technically limiting, and so identifying the cells with activated $G_s$-GPCR activity relies on the tTA transgene expression, since Rs1 shows too much similarity to endogenous serotonin receptors. In addition, while this study identified a clear role for Wnt ligands in driving a FD-like bone phenotype, the role of specific Wnt ligands, and how this correlates with FD bone lesions driven by activating GNAS mutations in humans, remains unclear. Finally, high doses of LGK974 were required to induce changes in the FD-like bone lesions in our mice, and those changes were not as dramatic of a reversal as seen in models where the $G_s$-GPCR pathway activity is normalized [15, 23]. This suggests that inhibiting Wnt pathway alone is insufficient for fully reversing FD bone lesions, and that directed reversal of $G_s$-GPCR pathway hyperactivity would be the best treatment strategies for FD. In addition, the high dose of 30mg/kg/day used can cause bone resorption in WT mice [68], thus limiting potential clinical utility.

# CHAPTER 3: Drug Repositioning to Identify Potential Drugs for Treating Fibrous Dysplasia

## INTRODUCTION

### Drug repositioning is a useful strategy for finding new therapeutic candidates.

The availability of "-omics" data provides a powerful opportunity to improve human health by using computational integrative methods to refine the current knowledge about disease mechanism, diagnostics, and therapeutics. Precision medicine approaches that integrate different types of multi-scale measurements have successfully identified biomarkers and therapeutic targets in other diseases. Kotelnikova et al developed and applied meta-analysis methods to identify novel drug targets and biomarkers in Duchenne Muscular Dystrophy [76]. Chen et al recently identified PTK7 as a survival biomarker using meta-analysis in lung cancer [77]. Others have proposed utilizing computational approaches for identification of biomarkers for bipolar disorder [78]. Here, we used diverse types of molecular data to inform therapeutic strategies in FD.

Genomic technologies allow us to extract large amounts of data from patient samples, elucidating previously unknown factors involved in disease such as drug targets or disease biomarkers. We will use the single cell signature we created to query publicly available drug gene expression resources such as the Connectivity Map (Cmap)

and LINCS data to identify drug repurposing and combination therapy candidates [79, 80]. CMap contains genomewide gene expression data on cell lines treated with over 1,000 compounds [81]. LINCS contains limited measurements of 1,000 genes across over 10,000 compounds measuring expression before and after treatment [80].

Drug repositioning takes established compounds and attempts to find new therapeutic indications for them. Drug repositioning offers several advantages over traditional drug development including reduced development costs and shorter paths to approval. Recent approaches to drug repositioning use high-throughput approaches to assess a compound's potential therapeutic qualities [43, 44].

The Sirota lab previously developed a systematic computational approach to predict novel therapeutic indications based on comprehensive testing of molecular signatures in drug-disease pairs. They experimentally validated a prediction for the anti-ulcer drug cimetidine as a candidate therapeutic agent in the treatment of lung adenocarcinoma, and demonstrated its efficacy both *in vitro* and *in vivo* using mouse xenograft models [82]. They also applied the computational approach to discover new drug therapies for inflammatory bowel disease (IBD) *in silico* [83]. Among the top compounds predicted to be therapeutic for IBD by Dr. Sirota's approach were prednisolone, a corticosteroid used to treat IBD, and topiramate, an anticonvulsant drug not previously described to have

efficacy for IBD or any related disorders of inflammation or the gastrointestinal tract. Using a trinitrobenzenesulfonic acid (TNBS)-induced rodent model of IBD, the team experimentally validated our topiramate prediction *in vivo* [83]. This work was published as two back-to-back papers in 2011 and has been well cited since the publication [82, 83]. This computational method provides a systematic approach for repositioning established drugs to treat a wide range of human diseases. We have used this approach to predict repurposed therapies for FD.

There are currently no effective medical treatments for FD. By identifying the gene profile of cells with activated $G_s$ signaling in FD and using a drug repositioning approach, we aim to discover pharmaceutical agents that could reverse the FD gene expression changes. Expression of osteoblastic genes [17] and microarray of genetically marked osteoblasts [84] suggest that a disease signature will be identifiable. Drugs that target the same genes as the FD gene profile, yet in a reversed expression pattern, may be useful for treating FD. The single cell sequencing technique allows us to utilize the drug repositioning analysis on a defined population of cells from both Coll(2.3)$^+$/Rs1$^+$ and control mice. Potential drugs that can be capable of inducing the opposite gene expression profile of FD have been identified to reverse the FD phenotype of the Coll(2.3)$^+$/Rs1$^+$ mouse.

## MATERIAL AND METHODS

### Drug repositioning pipeline

Drug repositioning analysis was performed by comparing the molecular profile--or disease signature--of FD with that of pharmacological agents in the Broad Institute's Connectivity Map database (CMap) [81]. The pipeline was based on one developed by the Bin Chen Lab [85, 86]. More specifically, we created the FD disease signature from our single cell data using the differential expression results from our cluster 8 Coll(2.3)$^{+}$/Rs1$^{+}$ versus control comparison. The results were ordered by most significant p-value. We then used for our FD signature the 150 top up-regulated and 150 top down-regulated differentially expressed genes. Our disease signature was queried against CMap's 6100 transcriptomic experiments with 1309 drugs. A rank normalization procedure was carried out to create a reference database of drug gene expression and a drug-disease score or 'CMap score' was assigned to each drug-disease pair based on profile similarity. We focused on investigating the top drug repositioning results with a q-value < 0.05 and negative CMap scores, as negative scores indicate a reversal of our signature by the compound or drug used in the CMap experiment. These parameters were used to create a list of candidate drugs that may target FD (Figure 3).

## RESULTS

The disease gene expression profile of FD were created by identifying up- or down-regulated gene expression in Coll(2.3)$^{+}$/Rs1$^{+}$ and control samples (Figure 2.1.1A-B). scRNAseq was performed and we chose cluster 8 which included the osteoblasts and has the highest number of differential expression (DE) genes. Drugs which have opposite gene expression signatures to FD were identified through our computational analysis using the Connectivity Map and LINCS databases (Figure 3).

The next steps in this work are to investigate the specific genes and pathways in the disease profile that are being reversed by the drug. The predicted compounds need to be tested for their ability to reverse the bone phenotype of the Coll(2.3)$^{+}$/Rs1$^{+}$ mice or human FD cells (Table 3) and also further evaluated in animal models in order to show whether they can alleviate the disease phenotype. Our previous study has demonstrated that the bone phenotype of the Coll(2.3)$^{+}$/Rs1$^{+}$ mice could be reversed by regulating the $G_s$ signaling[15]. Since the databases are based on FDA approved drugs, the drug candidates that were found may move quickly into pre-clinical and clinical testing while revealing disease mechanisms.

## DISCUSSION

Our initial analysis of the FD-like bone lesions of ColI(2.3)$^{+}$/Rs1$^{+}$ mice identified a number of medications that may be useful for reversing the “disease gene expression signature” in osteoblastic cells. Although our analysis was limited by the low number of cells, and by the relatively shallow depth of sequencing resulting from single cell analysis vs. bulk RNAseq analysis, we were still able to identify some candidate medications or drug classes with potential therapeutic impact. These include geldanamycin that targets HSP90, the sex hormone estriol, the NSAID acetylsalicylic acid, nicotinic acid and gossypol that target GPCRs, the anti-fungal drug trichostatin A, the steroids desoxycortone and triamcinolone, and carbamazepine that acts on the ion channel (Table 3). This work can further be expanded to include signatures from other relevant cell types and future testing of these medications in new *in vitro* and *in vivo* models will be useful for identifying their therapeutic potentials.

## CHAPTER 4: SUMMARY

This study uses a translational approach combining a unique mouse model of FD to elucidate the cellular interactions in FD and create a novel gene expression disease signature of FD. The results also showed that Wnt inhibition reversed some but not all features of established FD. Systemic Wnt inhibition would likely cause osteoporosis in normal bone and potential for widespread toxicity. Results from these studies will help provide a novel drug repositioning strategy to find FDA-approved candidate drugs that can potentially be repurposed for the treatment of FD. We will also collect pertinent patient samples to facilitate future validation of our results from the FD mouse model in human samples. This work expands our understanding of FD pathogenesis and helps identify potential strategies for treatment, laying a strong foundation for future research on GPCR signaling and bone development (Figure 4). The results from scRNAseq revealed that there are multiple sub-clusters within the osteoblast lineage, and further investigation may provide a more robust surface marker to identify osteoblasts for FACS isolation. Future directions also include testing candidate drugs identified by our drug repositioning studies in FD mouse model, biomechanical testing of the reversal bone, scRNAseq on drug-treated mice, drug repositioning on human FD samples, and combination therapy.

## FIGURES

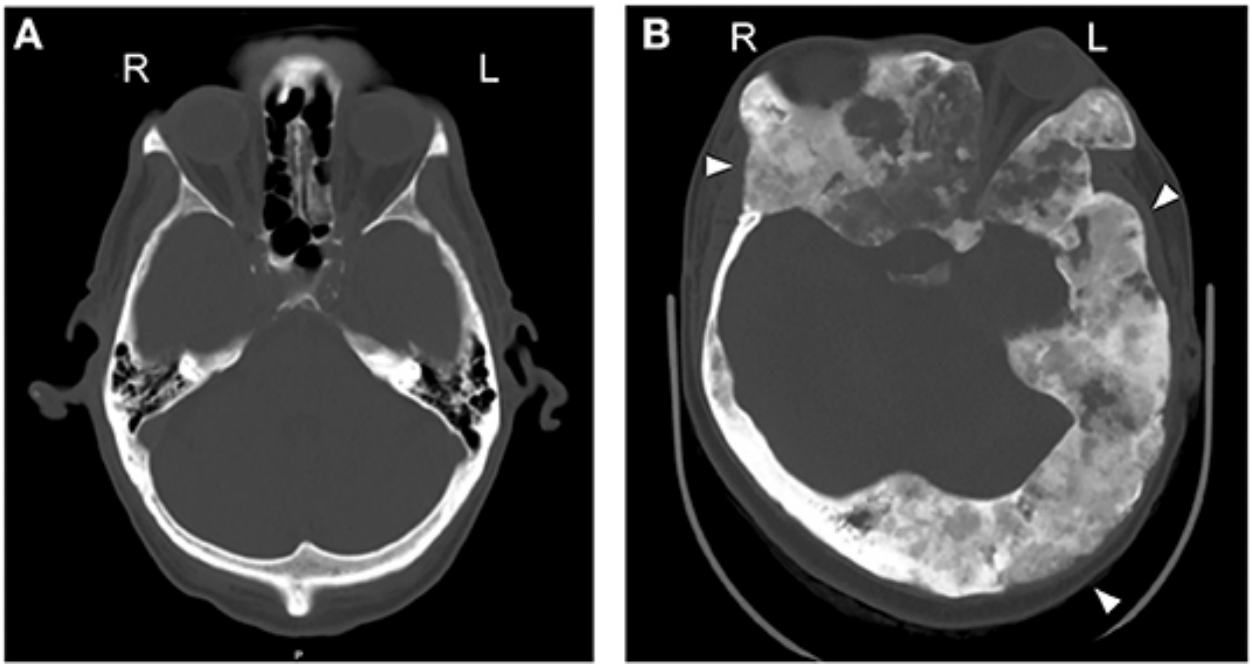


**Figure 1.1 Fibrous dysplasia commonly affects the skull and is mosaic.**

Axial CT across the orbit.

**(A)** A normal CT scan of the craniofacial bones, from a skeletally normal 61 y.o. male.

**(B)** A 29 y.o. female with craniofacial FD. Note the asymmetry in the skull: ground glass expanded left sided lesions, multiple ground glass lesions around the left orbit, and displaced globe (arrowheads) [87].

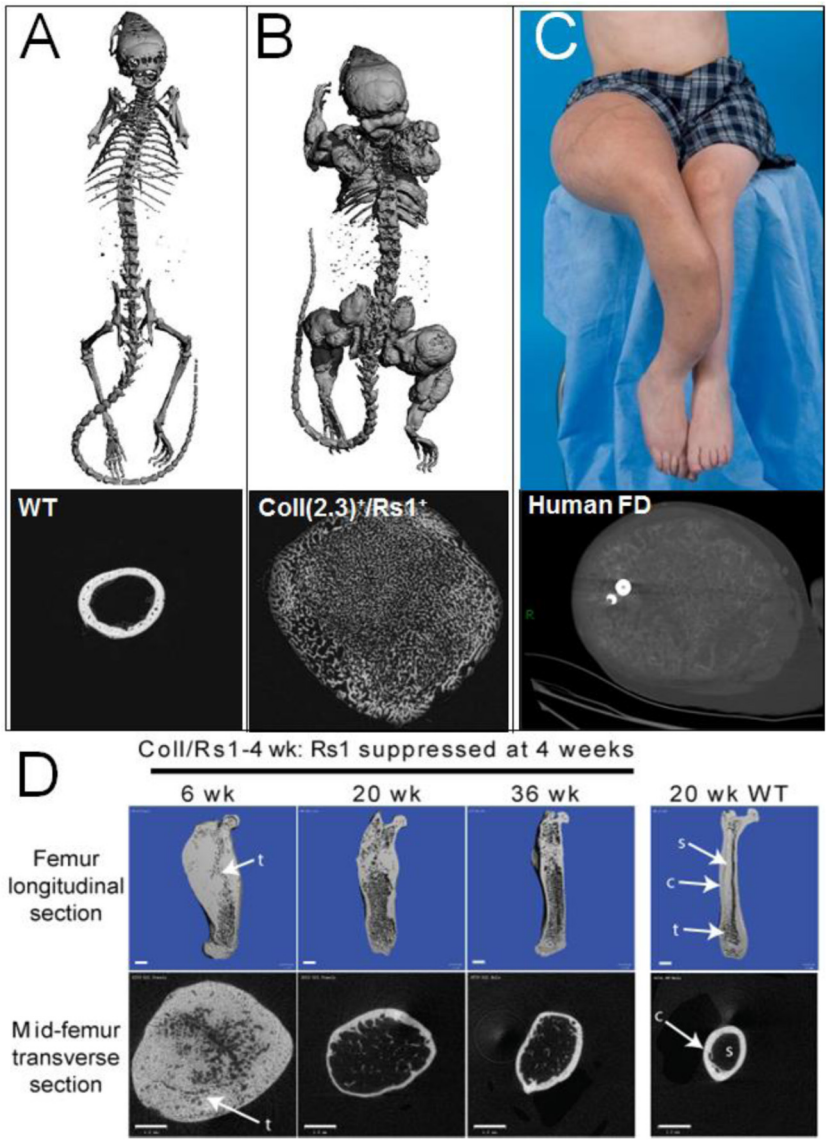


**Figure 1.2 Rs1-mediated $G_s$ activation in osteoblastic cells causes fibrous dysplasia.**

**(A)** 9-week old normal mouse. Mid-femur microCT cross sections are shown below.

**(B)** 9-week-old Coll(2.3)$^+$/Rs1$^+$ mouse with increased trabecular bone resembling FD.

**(C)** Patient with severe FD showing similar trabecularization in the femur. Clinical image from M. Collins [88].

**(D)** Suppressing $G_s$-GPCR activity in osteoblasts can reverse the FD bone lesions. s, bone marrow space; c, cortical bone, t, trabecular bone. Scale bar, 1 mm. Images were previously published in [15, 21].

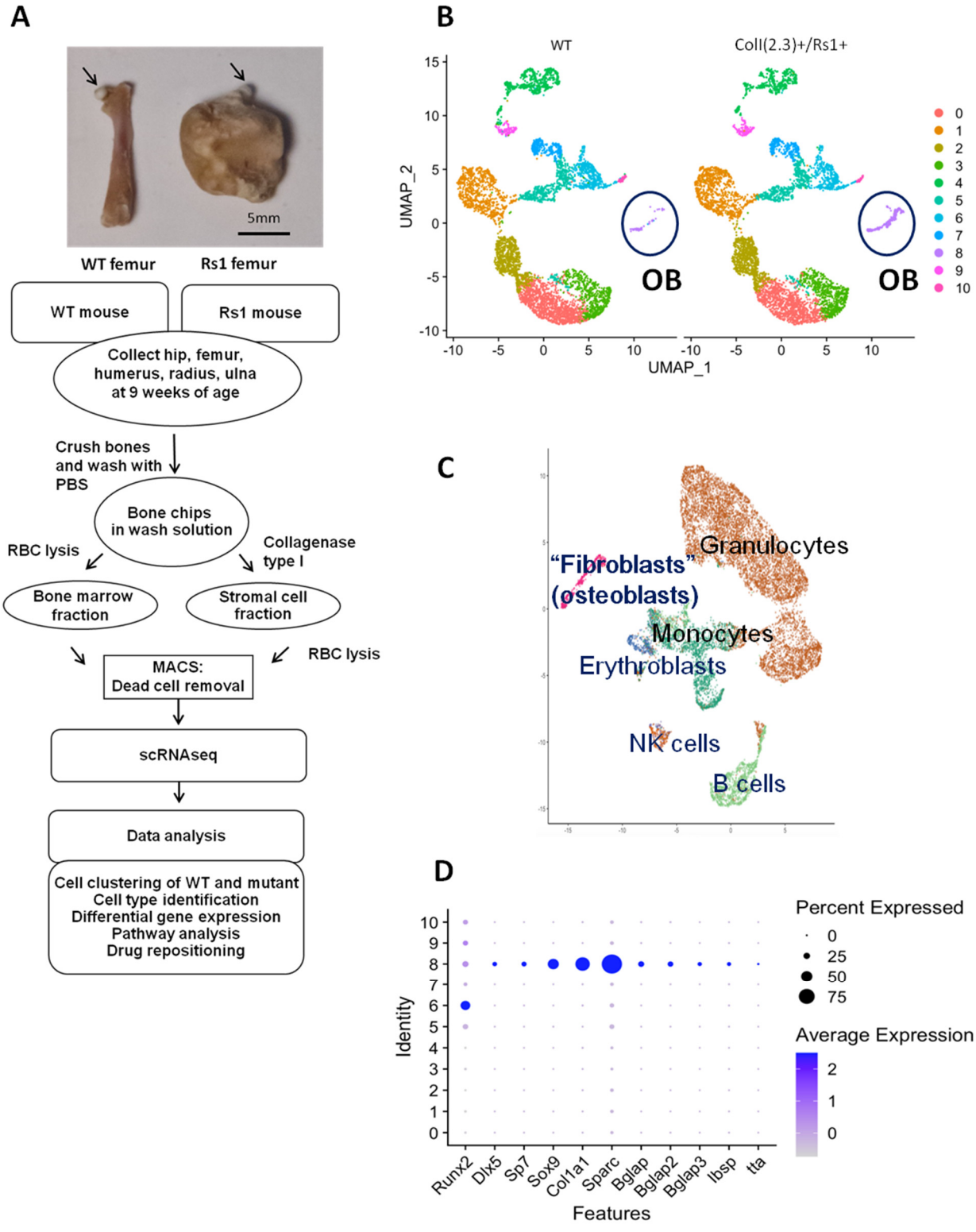
A
5mm
WT femur
Rs1 femur
WT mouse
Rs1 mouse
Collect hip, femur, humerus, radius, ulna at 9 weeks of age
Crush bones and wash with PBS
Bone chips in wash solution
RBC lysis
Collagenase type I
Bone marrow fraction
Stromal cell fraction
RBC lysis
MACS: Dead cell removal
scRNAseq
Data analysis
Cell clustering of WT and mutant
Cell type identification
Differential gene expression
Pathway analysis
Drug repositioning
B
WT
Coll(2.3)+/Rs1+
UMAP_2
UMAP_1
OB
OB
0
1
2
3
4
5
6
7
8
9
10
C
"Fibroblasts" (osteoblasts)
Granulocytes
Monocytes
Erythroblasts
NK cells
B cells
D
Identity
Features
Runx2
Dlx5
Sp7
Sox9
Col1a1
Sparc
Bglap
Bglap2
Bglap3
Ibsp
tta
Percent Expressed
0
25
50
75
Average Expression
2
1
0

**Figure 2.1.1. scRNAseq cell cluster analyses identifies differences in osteoblast populations between WT and ColI(2.3)+/Rs1+.**

**(A)** ColI(2.3)+/Rs1+ mouse model and tissue processing to collect cells for scRNAseq. 9 week old WT and ColI(2.3)$^{+}$/Rs1$^{+}$ male mice, 2 of each, hip, femur, tibia, fibular, humerus, radius, ulnar bones were isolated, crushed and washed with PBS. The wash solution was treated with RBC lysis and the cells were collected as the bone marrow fraction. The bone chips were incubated with Collagenase Type I solution to release the stromal cells, treated with RBC lysis, then the cells were collected as the stromal cell fraction. Both the bone marrow and stromal cell fraction were followed by the dead cell removal procedure using magnetic activated cell sorting (MACS) before sent for single-cell RNA sequencing (scRNAseq).

**(B)** Comparison of combined WT and combined ColI(2.3)$^{+}$/Rs1$^{+}$ cell clusters shows plot difference in cluster 8. n=2 WT, n=2 ColI(2.3)$^{+}$/Rs1$^{+}$.

**(C)** The cell types of each cluster in all 4 samples combined (2 WT, 2 ColI(2.3)$^{+}$/Rs1$^{+}$) were identified by using SingleR to match to existing databases.

**(D)** Expression of known bone markers Sp7,Col1α1, Bglap2, Ibsp in each cluster (0-10) of all 4 samples combined. Expressions of the genes are highest in cluster 8. Expression of Runx2, Col1α1, Ibsp, Sox9, Sp7, and Bglap2 in combined ColI(2.3)$^{+}$/Rs1$^{+}$ and combined WT cells showed higher Col1α1 and Ibsp expression in ColI(2.3)$^{+}$/Rs1$^{+}$ cells.

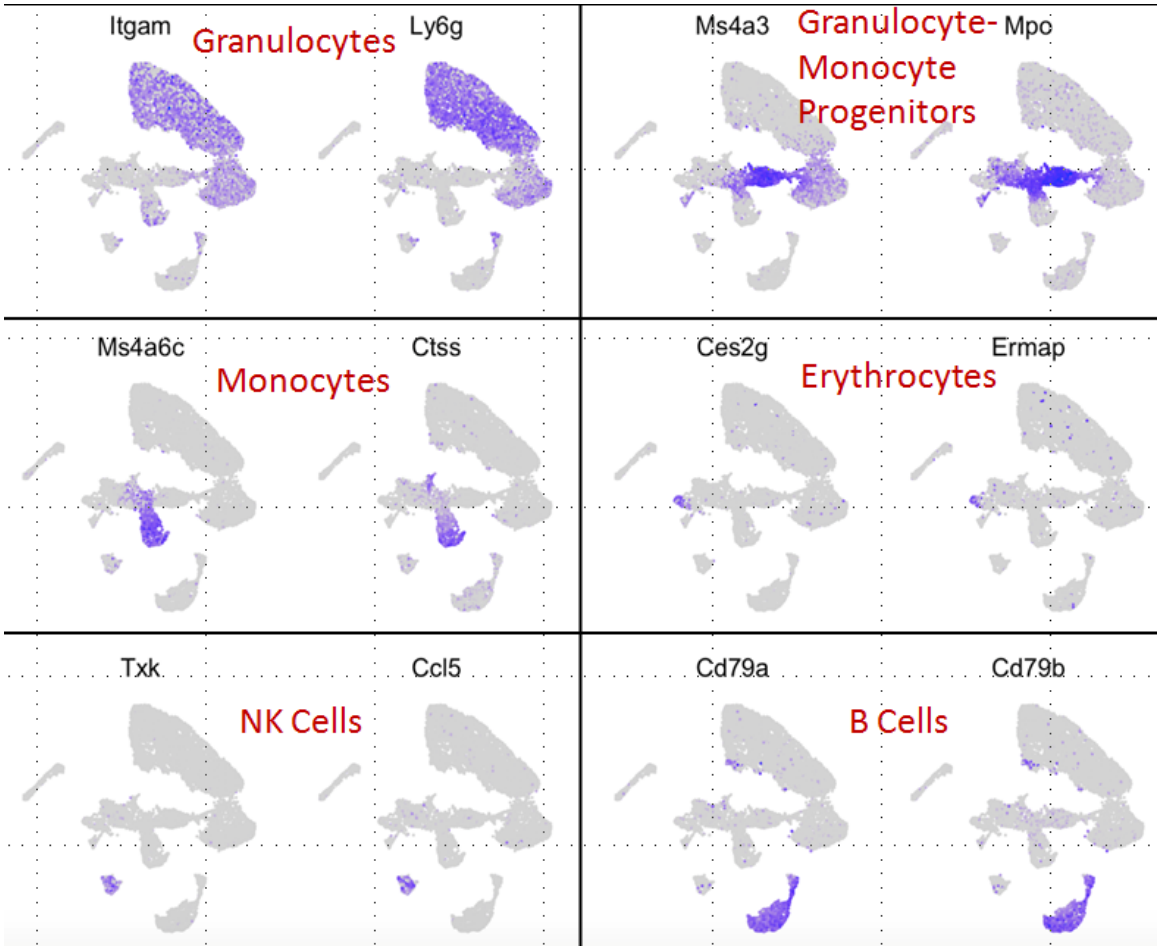


**Figure 2.1.2. Validating cell types with known markers.**

Using known markers of granulocytes, monocytes, erythorocytes, NK cells and B cells to validate the cell types of each cluster in all 4 samples combined. These results correspond with the results from SingleR.

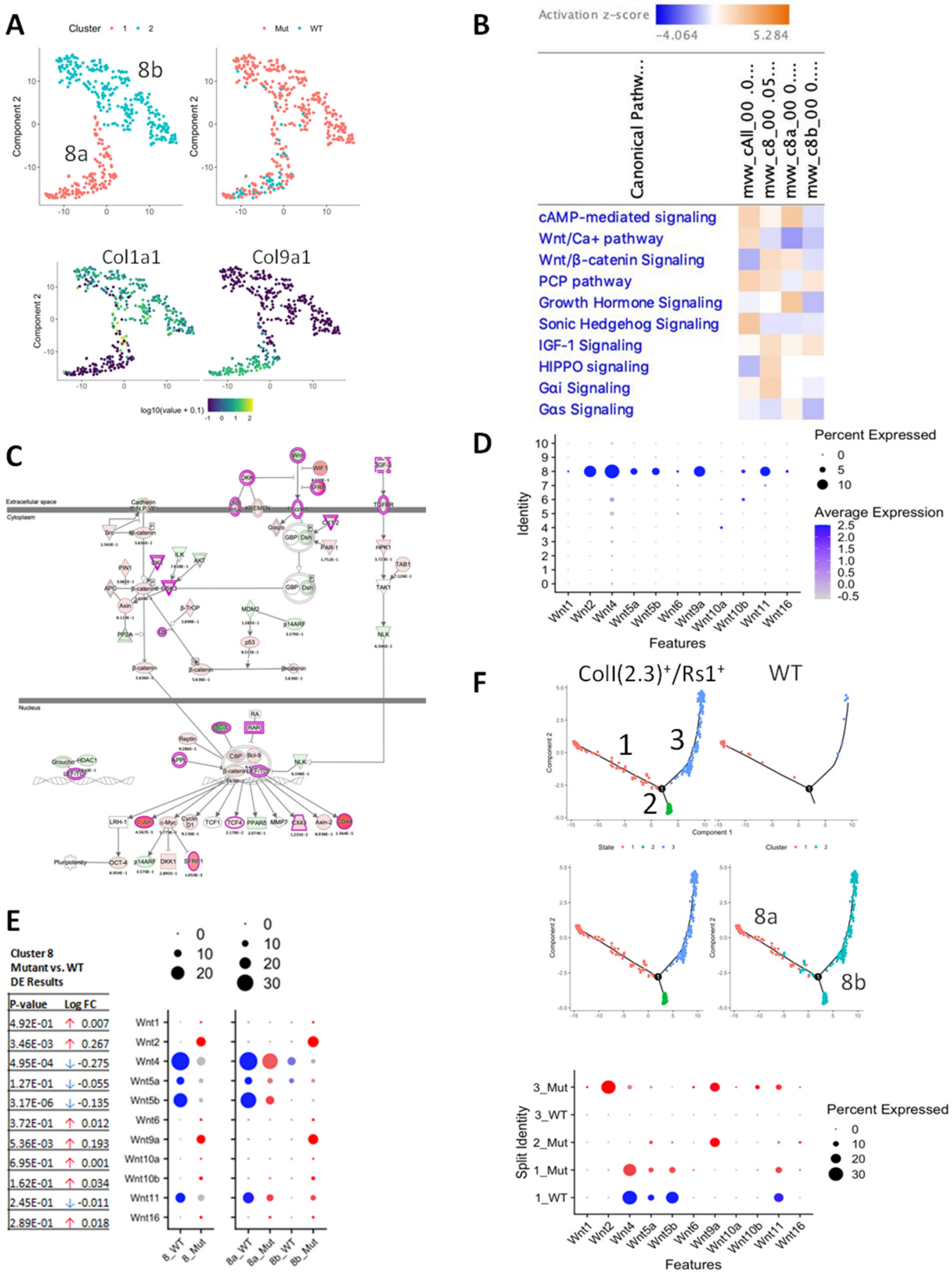
A
Cluster 1 2
Mut WT
8b
8a
Component 2
Col1a1
Col9a1
log10(value + 0.1)
B
Activation z-score
-4.064
5.284
Canonical Pathw...
mvw_cAll_00 .0...
mvw_c8_00 .05...
mvw_c8a_00 0....
mvw_c8b_00 0....
cAMP-mediated signaling
Wnt/Ca+ pathway
Wnt/β-catenin Signaling
PCP pathway
Growth Hormone Signaling
Sonic Hedgehog Signaling
IGF-1 Signaling
HIPPO signaling
Gαi Signaling
Gαs Signaling
C
Extracellular space
Cytoplasm
Nucleus
D
Percent Expressed
Average Expression
Identity
Features
Wnt1 Wnt2 Wnt4 Wnt5a Wnt5b Wnt6 Wnt9a Wnt10a Wnt10b Wnt11 Wnt16
E
Cluster 8
Mutant vs. WT
DE Results
P-value Log FC
4.92E-01 ↑ 0.007
3.46E-03 ↑ 0.267
4.95E-04 ↓ -0.275
1.27E-01 ↓ -0.055
3.17E-06 ↓ -0.135
3.72E-01 ↑ 0.012
5.36E-03 ↑ 0.193
6.95E-01 ↑ 0.001
1.62E-01 ↑ 0.034
2.45E-01 ↓ -0.011
2.89E-01 ↑ 0.018
8_WT 8_Mut 8a_WT 8a_Mut 8b_WT 8b_Mut
F
Coll(2.3)+/Rs1+
WT
1
2
3
Component 1
Component 2
State
Cluster
8a
8b
Split Identity
3_Mut 3_WT 2_Mut 1_Mut 1_WT
Percent Expressed
Features

**Figure 2.2.1. Wnt expression in stromal cell fraction is present in osteoblasts and other cell types.**

**(A)** Subclustering cluster 8 resulted in cluster 8a with higher expression of Col9α1, and cluster 8b with higher expression of Col1α1.

**(B)** In the up-regulated genes of ColI(2.3)$^{+}$/Rs1$^{+}$ cells, we found that Igf1 (Insulin-like growth factor I) and other Igf binding proteins were in the center and interacted with various genes. We also found up-regulated Wnt pathway genes, such as Serpinf1, Sfrp4, Jun, which supports our hypothesis. Hedgehog signaling pathway (WP116), Wnt signaling pathway (WP403), and G protein signaling pathways (WP232) are in the result pathways from WikiPathways 2019 Mouse. KEGG 2019 Mouse showed Wnt signaling pathway and hedgehog signaling pathway. Wnt genes that were identified in cluster 8 include Wnt1, 2, 4, 5a, 5b, 6, 9a, 10a, 10b, 11, 16 (11 genes). Wnt signaling in kidney disease (WP3857) and basal cell carcinoma are the top 1 pathway on WikiPathways 2019 Mouse and KEGG 2019 Mouse, respectively.

**(C)** Ingenuity pathway analysis (IPA) of the osteoblast cluster (cluster 8), ColI(2.3)$^{+}$/Rs1$^{+}$ vs WT, with a p-value cutoff of 0.05 showed the differential expression genes that are in the Wnt/β-catenin signaling pathway, Wnt4 and Wnt5b is down-regulated in ColI(2.3)$^{+}$/Rs1$^{+}$ cells, while Wnt2 and Wnt9a is up-regulated in ColI(2.3)$^{+}$/Rs1$^{+}$ cells. Sox5, Sox6, Sox8 and Sox9 are down-regulated in the ColI(2.3)$^{+}$/Rs1$^{+}$ cells. Lrp1, c-Jun, Sfrp1, and CD44 are highly up-regulated in the ColI(2.3)$^{+}$/Rs1$^{+}$ cells.

**(D)** The dot plot shows gene expression in each cluster (0-10) of WT and ColI(2.3)$^{+}$/Rs1$^{+}$ cells respectively. Cluster 8 includes osteoblasts. Expressions of Wnt6, Wnt10a, Wnt10b appears in the osteoblast cluster (cluster 8) and other clusters. Expressions of Wnt1, Wnt2, Wnt9a and Wnt16 in each cluster, and only appearing in the ColI(2.3)$^{+}$/Rs1$^{+}$ cells, and also expressed highest in cluster 8.

**(E)** The dot plot shows differential expression of Wnt ligands in ColI(2.3)$^{+}$/Rs1$^{+}$ vs WT.

**(F)** Analyses from Monocle showed that the osteoblast cluster (cluster 8) branches into red (1), green (2), and blue (3) branches. As most of the WT that branch off are in the red and blue clusters, we assume that these paths are a more normal route for cell trajectory. The dot plot shows Wnt ligand gene expression in each branch.

# Wnt/β-catenin Pathway Genes

## "**Expected Up**" Genes

**Cluster 8**
**Mutant vs. WT**
**DE Results**

| P-value | Log FC | |
|---|---|---|
| 1.56E-05 | ↑ | 0.759 |
| 4.57E-05 | ↑ | 0.682 |
| 4.09E-07 | ↑ | 0.624 |
| 8.61E-05 | ↑ | 0.361 |
| 2.59E-03 | ↑ | 0.284 |
| 3.46E-03 | ↑ | 0.267 |
| 1.81E-02 | ↑ | 0.204 |
| 5.36E-03 | ↑ | 0.193 |
| 1.23E-02 | ↑ | 0.18 |
| 3.24E-02 | ↑ | 0.166 |
| 2.75E-02 | ↑ | 0.158 |
| 2.18E-02 | ↑ | 0.139 |
| 1.07E-01 | ↑ | 0.119 |
| 1.32E-01 | ↑ | 0.103 |
| 1.88E-01 | ↑ | 0.102 |
| 4.68E-01 | ↑ | 0.1 |
| 2.12E-01 | ↑ | 0.099 |
| 1.75E-01 | ↑ | 0.095 |
| 6.35E-01 | ↑ | 0.087 |
| 3.36E-01 | ↑ | 0.083 |
| 7.01E-01 | ↑ | 0.075 |
| 9.51E-01 | ↑ | 0.07 |
| 3.90E-01 | ↑ | 0.066 |
| 9.16E-01 | ↑ | 0.061 |
| 5.78E-01 | ↑ | 0.053 |
| 9.43E-02 | ↑ | 0.042 |
| 5.64E-01 | ↑ | 0.038 |
| 2.89E-01 | ↑ | 0.036 |
| 1.62E-01 | ↑ | 0.034 |
| 2.04E-01 | ↑ | 0.03 |
| 9.48E-01 | ↑ | 0.026 |
| 3.06E-01 | ↑ | 0.023 |
| 8.94E-01 | ↑ | 0.023 |
| 3.28E-01 | ↑ | 0.022 |
| 9.03E-01 | ↑ | 0.022 |
| 2.89E-01 | ↑ | 0.018 |
| 3.72E-01 | ↑ | 0.012 |
| 6.26E-01 | ↑ | 0.011 |
| 8.41E-01 | ↑ | 0.011 |
| 4.92E-01 | ↑ | 0.007 |
| 4.48E-01 | ↑ | 0.006 |
| 9.66E-01 | ↑ | 0.004 |
| 6.95E-01 | ↑ | 0.001 |
| 5.21E-01 | ↓ | -0.009 |
| 1.64E-01 | ↓ | -0.01 |
| 2.45E-01 | ↓ | -0.011 |
| 1.62E-01 | ↓ | -0.015 |
| 5.21E-01 | ↓ | -0.016 |
| 9.08E-01 | ↓ | -0.02 |
| 1.86E-01 | ↓ | -0.035 |
| 2.84E-01 | ↓ | -0.038 |
| 6.93E-01 | ↓ | -0.039 |
| 3.67E-01 | ↓ | -0.04 |
| 1.01E-01 | ↓ | -0.05 |
| 1.27E-01 | ↓ | -0.055 |
| 9.76E-01 | ↓ | -0.064 |
| 8.11E-02 | ↓ | -0.075 |
| 8.00E-02 | ↓ | -0.094 |
| 6.84E-04 | ↓ | -0.103 |
| 3.17E-06 | ↓ | -0.135 |
| 4.95E-04 | ↓ | -0.275 |

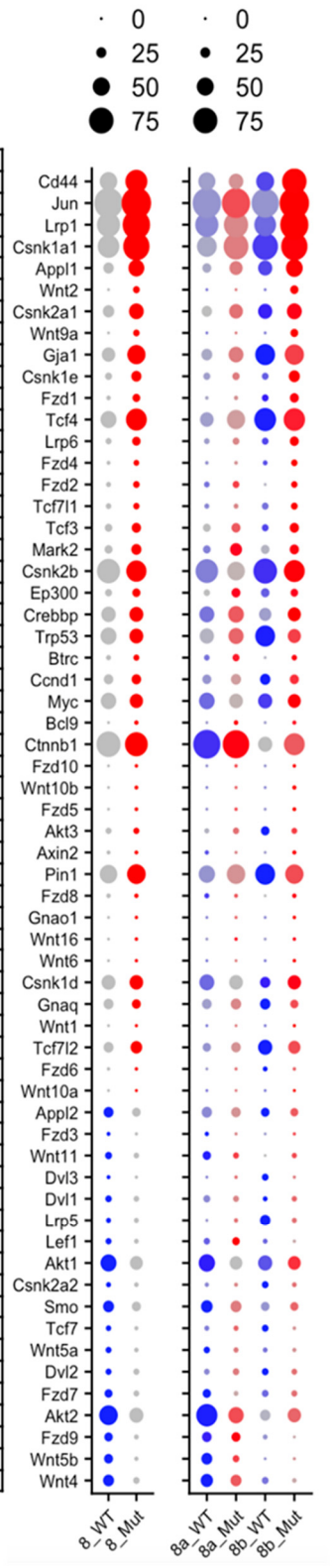


## "**Expected Down**" Genes

**Cluster 8**
**Mutant vs. WT**
**DE Results**

| P-value | Log FC | |
|---|---|---|
| 4.10E-06 | ↑ | 1.731 |
| 1.05E-03 | ↑ | 0.493 |
| 1.36E-04 | ↑ | 0.445 |
| 8.55E-01 | ↑ | 0.433 |
| 1.99E-03 | ↑ | 0.303 |
| 7.24E-04 | ↑ | 0.298 |
| 4.16E-04 | ↑ | 0.297 |
| 6.42E-03 | ↑ | 0.271 |
| 1.30E-01 | ↑ | 0.246 |
| 6.16E-02 | ↑ | 0.197 |
| 4.69E-02 | ↑ | 0.184 |
| 3.23E-02 | ↑ | 0.182 |
| 3.73E-01 | ↑ | 0.168 |
| 7.51E-01 | ↑ | 0.145 |
| 2.24E-01 | ↑ | 0.117 |
| 3.95E-01 | ↑ | 0.108 |
| 7.61E-01 | ↑ | 0.09 |
| 7.15E-01 | ↑ | 0.078 |
| 5.52E-02 | ↑ | 0.071 |
| 4.87E-01 | ↑ | 0.071 |
| 4.77E-01 | ↑ | 0.069 |
| 2.49E-01 | ↑ | 0.064 |
| 7.59E-01 | ↑ | 0.054 |
| 1.56E-01 | ↑ | 0.05 |
| 1.37E-01 | ↑ | 0.043 |
| 2.89E-01 | ↑ | 0.042 |
| 7.80E-01 | ↑ | 0.039 |
| 2.28E-01 | ↑ | 0.038 |
| 9.29E-01 | ↑ | 0.036 |
| 8.15E-01 | ↑ | 0.033 |
| 8.11E-01 | ↑ | 0.023 |
| 8.52E-01 | ↑ | 0.022 |
| 5.76E-01 | ↑ | 0.016 |
| 2.89E-01 | ↑ | 0.014 |
| 4.26E-01 | ↑ | 0.012 |
| 4.26E-01 | ↑ | 0.011 |
| 6.62E-01 | ↑ | 0.011 |
| 4.26E-01 | ↑ | 0.008 |
| 3.72E-01 | ↑ | 0.006 |
| 5.76E-01 | ↑ | 0.003 |
| 6.51E-01 | ↓ | -0.002 |
| 8.27E-01 | ↓ | -0.005 |
| 1.23E-02 | ↓ | -0.007 |
| 2.00E-01 | ↓ | -0.01 |
| 5.41E-01 | ↓ | -0.018 |
| 1.95E-01 | ↓ | -0.019 |
| 1.35E-01 | ↓ | -0.02 |
| 9.01E-01 | ↓ | -0.02 |
| 1.25E-02 | ↓ | -0.037 |
| 1.64E-01 | ↓ | -0.079 |
| 2.31E-02 | ↓ | -0.103 |
| 1.77E-01 | ↓ | -0.111 |
| 9.20E-07 | ↓ | -0.198 |
| 2.18E-08 | ↓ | -0.248 |
| 4.20E-04 | ↓ | -0.271 |
| 2.01E-12 | ↓ | -0.879 |

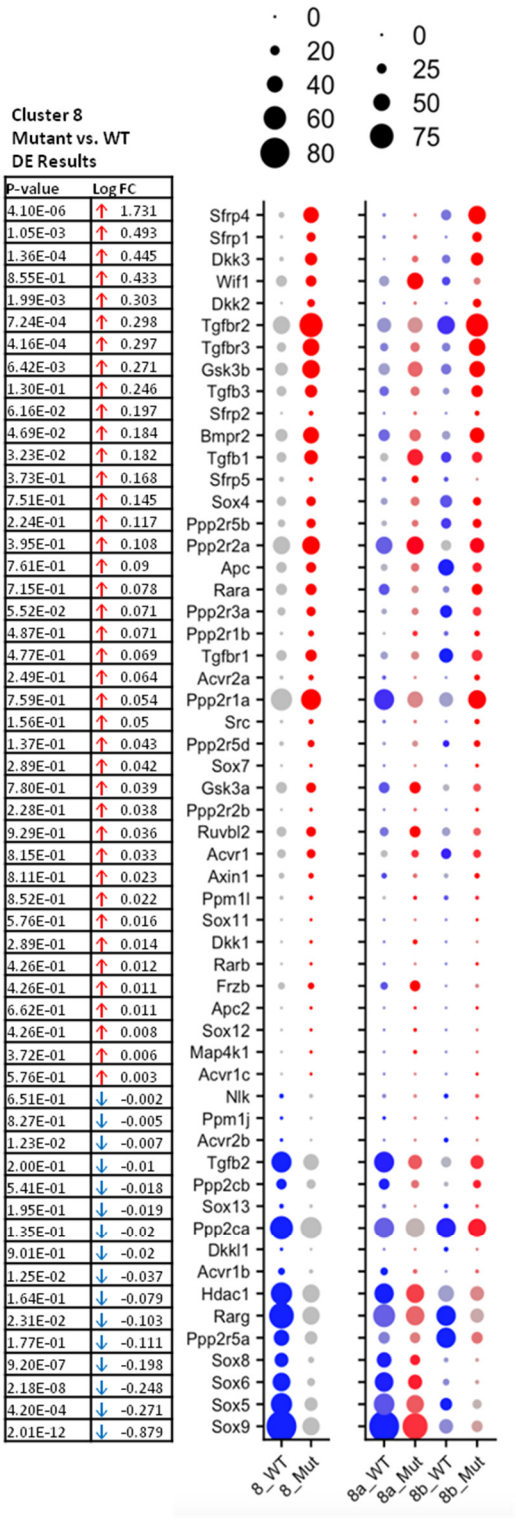

**Figure 2.2.2. Coll(2.3)$^{+}$/Rs1$^{+}$ expression of genes in the Wnt/β-catenin pathway.** "ExpectedUp" genes are genes that are expected to be up-regulated when the Wnt/β-catenin pathway is activated; "ExpectedDown" are genes that are expected to be down-regulated when the Wnt/β-catenin pathway is activated. Genes are arranged from highest log fold change to lowest log fold change. P value < 0.05. The size of the dot shows the percentage of cells that express that gene.

# IGF-1 Pathway Genes

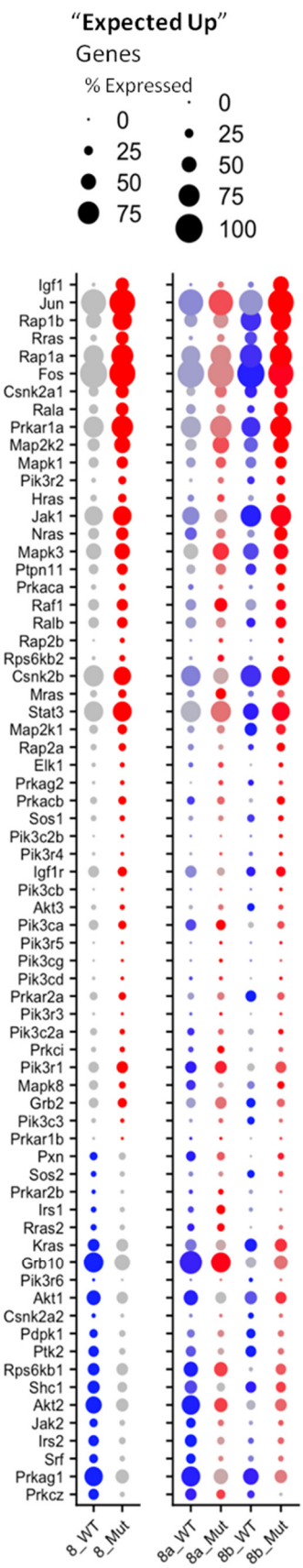


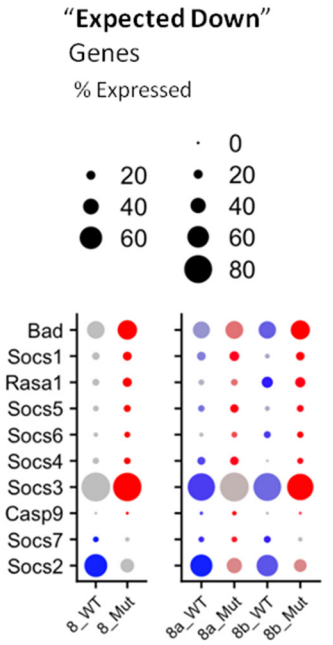


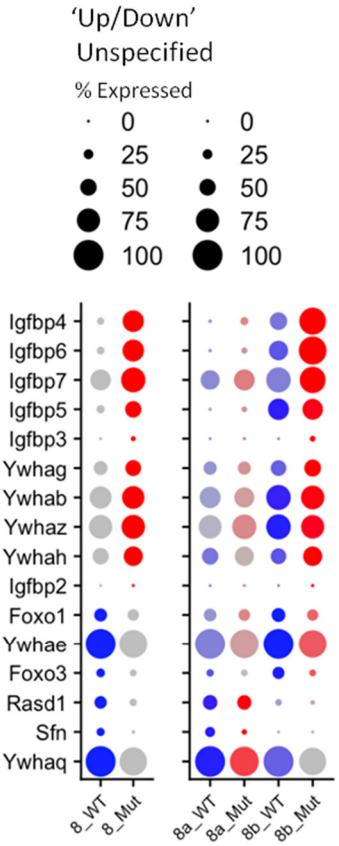

**Figure 2.2.3. ColI(2.3)$^{+}$/Rs1$^{+}$ expression of genes in the Igf-1 pathway.**
"ExpectedUp" genes are genes that are expected to be up-regulated when the Igf1 pathway is activated; "ExpectedDown" are genes that are expected to be down-regulated when the Igf1 pathway is activated. Genes are arranged from highest log fold change to lowest log fold change. P value < 0.05. The size of the dot shows the percentage of cells that express that gene. Igf1 is higher expressed (logFC) in ColI(2.3)$^{+}$/Rs1$^{+}$ cells and the percentage of cells that express Igf1 are larger. Although the level of expression of Jun is increased, the number of cells that express Jun is similar to WT cells.

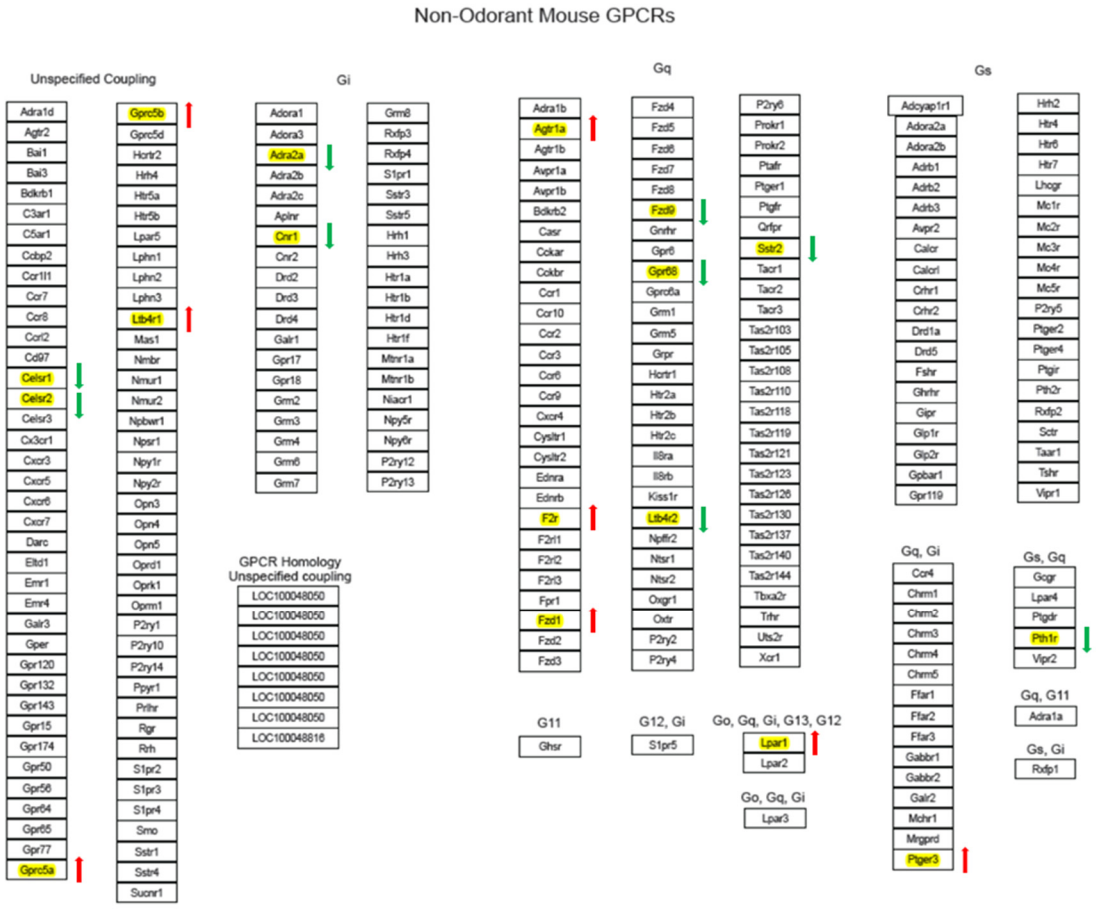


**Figure 2.2.4. Coll(2.3)$^{+}$/Rs1$^{+}$expression of non-odorant mouse GPCR genes.**

Gene expression analysis of the osteoblastic cell cluster (cluster 8), focusing on known G-protein coupled receptors. Red: up-regulated in Coll(2.3)$^{+}$/Rs1$^{+}$ cells; Green: down-regulated in Coll(2.3)$^{+}$/Rs1$^{+}$ cells; Pth1r is decreased in cluster 8 Coll(2.3)$^{+}$/Rs1$^{+}$ cells.

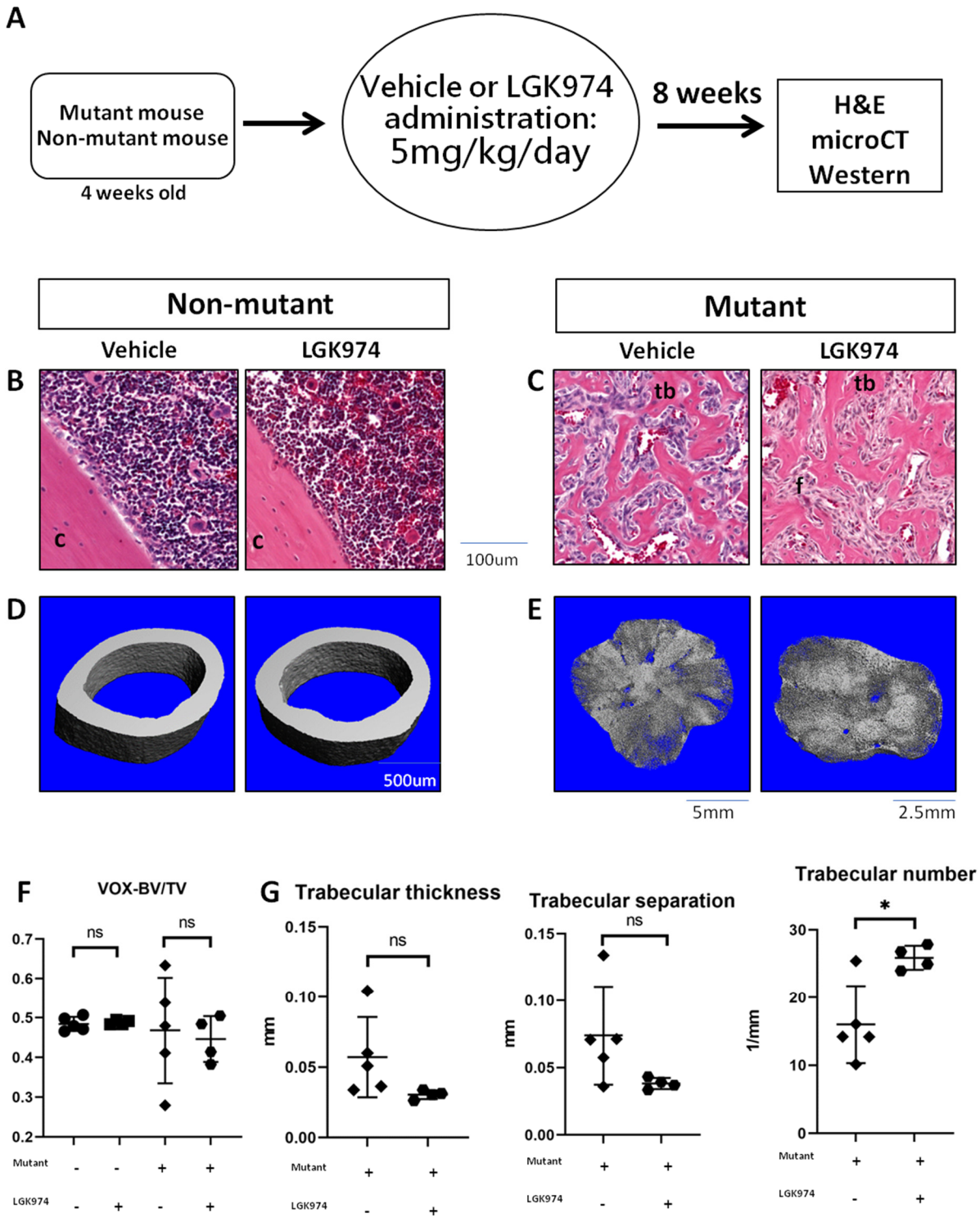
A
Mutant mouse
Non-mutant mouse
4 weeks old
Vehicle or LGK974 administration: 5mg/kg/day
8 weeks
H&E
microCT
Western
Non-mutant
Mutant
Vehicle
LGK974
B
C
tb
f
c
100um
D
E
500um
5mm
2.5mm
F
VOX-BV/TV
ns
Mutant
LGK974
G
Trabecular thickness
Trabecular separation
Trabecular number
mm
1/mm
*

**Figure 2.3. LGK974 low-dose experiment shows slight thinning of fibrous dysplastic trabecular bone.**

**(A)** Experimental flow of 4-week-old mutant and non-mutant mice, treated with vehicle or LGK974 5 mg/kg/day via oral gavage for 8 weeks.

**(B)** H&E staining of non-mutant femurs longitudinal-sectioned. (tb=trabecular bone; c=cortical bone, f=fibrous tissue)

**(C)** H&E staining of mutant femurs longitudinal-sectioned shows slight thinning of the trabecular bone that occupied the bone marrow space.

**(D)** 3D reconstruction of CT images of non-mutant mid-femur cross-sections at 5um resolution of the cortical bone.

**(E)** 3D reconstruction of CT images of mutant mid-femur cross-sections at 5um resolution, with trabecular bone in the bone marrow space visible.

**(F)** CT analyses of non-mutant and mutant mice show no significant difference of BV/TV ratio after LGK974 treatment. n=5 non-mutant with vehicle, n=4 non-mutant with drug; n=5 mutant with vehicle, n=4 mutant with drug; *: $p<0.05$, ns: not significant.

**(G)** CT analyses of $Col\text{I}(2.3)^{+}/Rs1^{+}$ mice show no significant difference of trabecular thickness after LGK974 treatment, while there was a significant increase in trabecular number. n=5 mutant with vehicle, n=4 mutant with drug; *: $p<0.05$, ns: not significant.

Non-mutant: WT, Col1 single transgenic, Rs1 single transgenic Mutant: $Col\text{I}(2.3)^{+}/Rs1^{+}$ mice (Rs1).

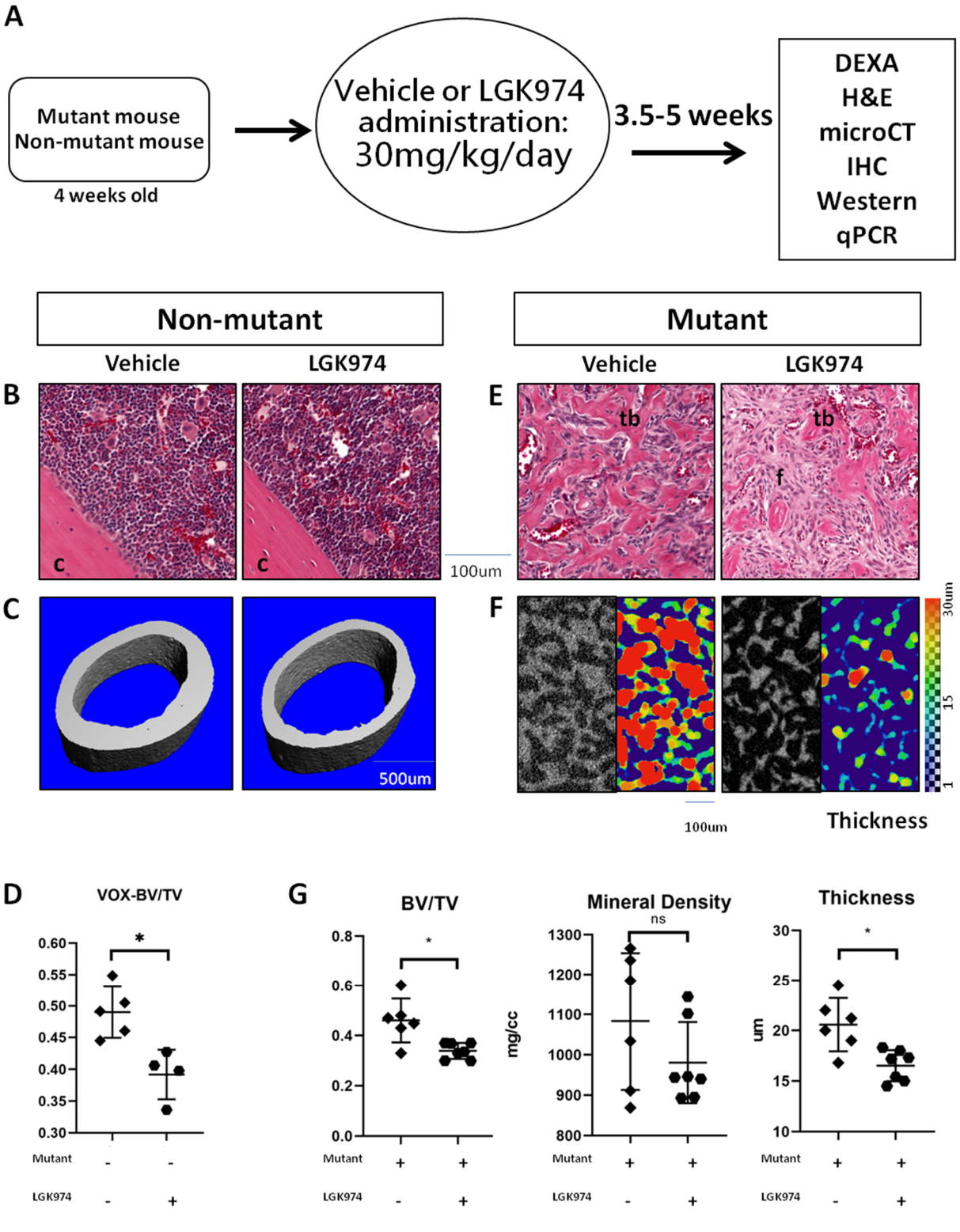
A
Mutant mouse
Non-mutant mouse
4 weeks old
Vehicle or LGK974 administration: 30mg/kg/day
3.5-5 weeks
DEXA
H&E
microCT
IHC
Western
qPCR
Non-mutant
Mutant
Vehicle
LGK974
Vehicle
LGK974
B
E
c
c
tb
tb
f
100um
C
F
500um
100um
30um
15
1
Thickness
D
VOX-BV/TV
0.60
0.55
0.50
0.45
0.40
0.35
0.30
*
Mutant - -
LGK974 - +
G
BV/TV
0.8
0.6
0.4
0.2
0.0
*
mg/cc
Mutant + +
LGK974 - +
Mineral Density
ns
1300
1200
1100
1000
900
800
Mutant + +
LGK974 - +
Thickness
30
25
20
15
10
um
*
Mutant + +
LGK974 - +

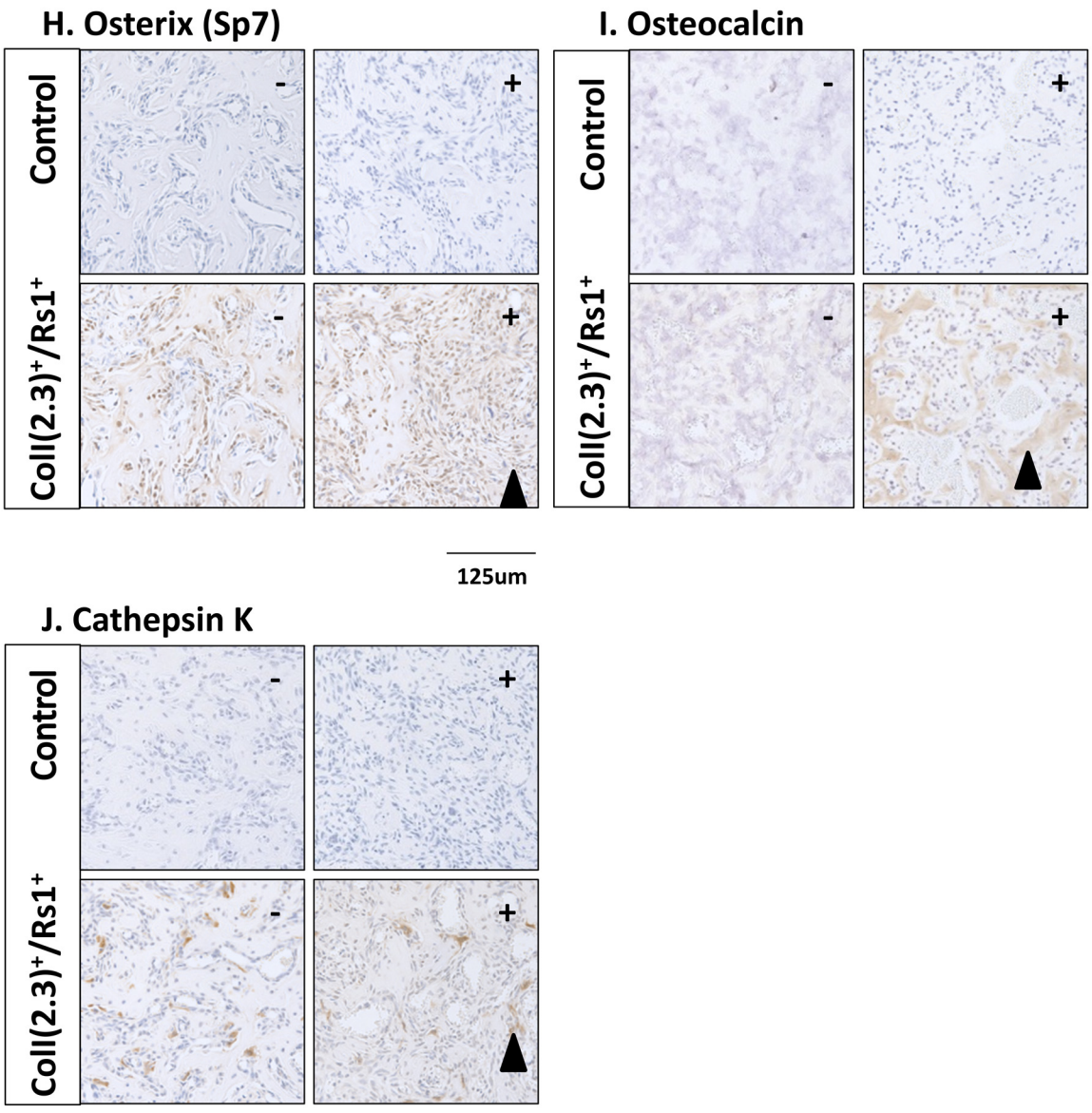
H. Osterix (Sp7)
I. Osteocalcin
Control
Coll(2.3)+/Rs1+
-
+
125um
J. Cathepsin K

**Figure 2.4.1. LGK974 high-dose experiment shows significant thinning of fibrous dysplastic trabecular bone.**

**(A)** Experiment flow of 4-week-old mutant and non-mutant mice, treated with vehicle or LGK974 30mg/kg/day via oral gavage for 3.5-5 weeks.

**(B)** H&E staining of non-mutant femurs longitudinal-sectioned. (tb=trabecular bone; c=cortical bone, f=fibrous tissue)

**(C)** 3D reconstruction of CT images of non-mutant mid-femur cross-sections at 5um resolution show thinning of the cortical bone after LGK974 administration.

**(D)** CT analysis of non-mutant mice shows significant decrease of BV/TV ratio after LGK974 administration. n=5 non-mutant with vehicle, n=4 non-mutant with drug; *: $p<0.05$, ns: not significant.

**(E)** H&E staining of mutant femurs longitudinal-sectioned shows thinning of the trabecular bone that occupied the bone marrow space.

**(F)** CT images of mutant femur at 2um resolution show thinning of the trabecular bone, with thickness up to 30um. Since the microCT resolution is 2um voxel, the minimum thickness of the bone thickness measured is 2um.

**(G)** CT analysis of mutant mice shows significant decrease of BV/TV ratio and thickness after LGK974 administration, while there was no significant difference in mineral density. n=6 mutant with vehicle, n=7 mutant with drug; *: $p<0.05$, ns: not significant.

**(H)** IHC Sp7 staining: Sp7- positive cells are present after LGK974 treatment (arrow).

**(I)** IHC Osteocalcin: osteocalcin is present in the matrix (arrow).

**(J)** IHC Cathepsin K: osteoclasts are present after LGK974 administration (arrow). Non-mutant: WT, Col1 single transgenic, Rs1 single transgenic; Mutant: $ColI(2.3)^{+}/Rs1^{+}$ mice (Rs1).

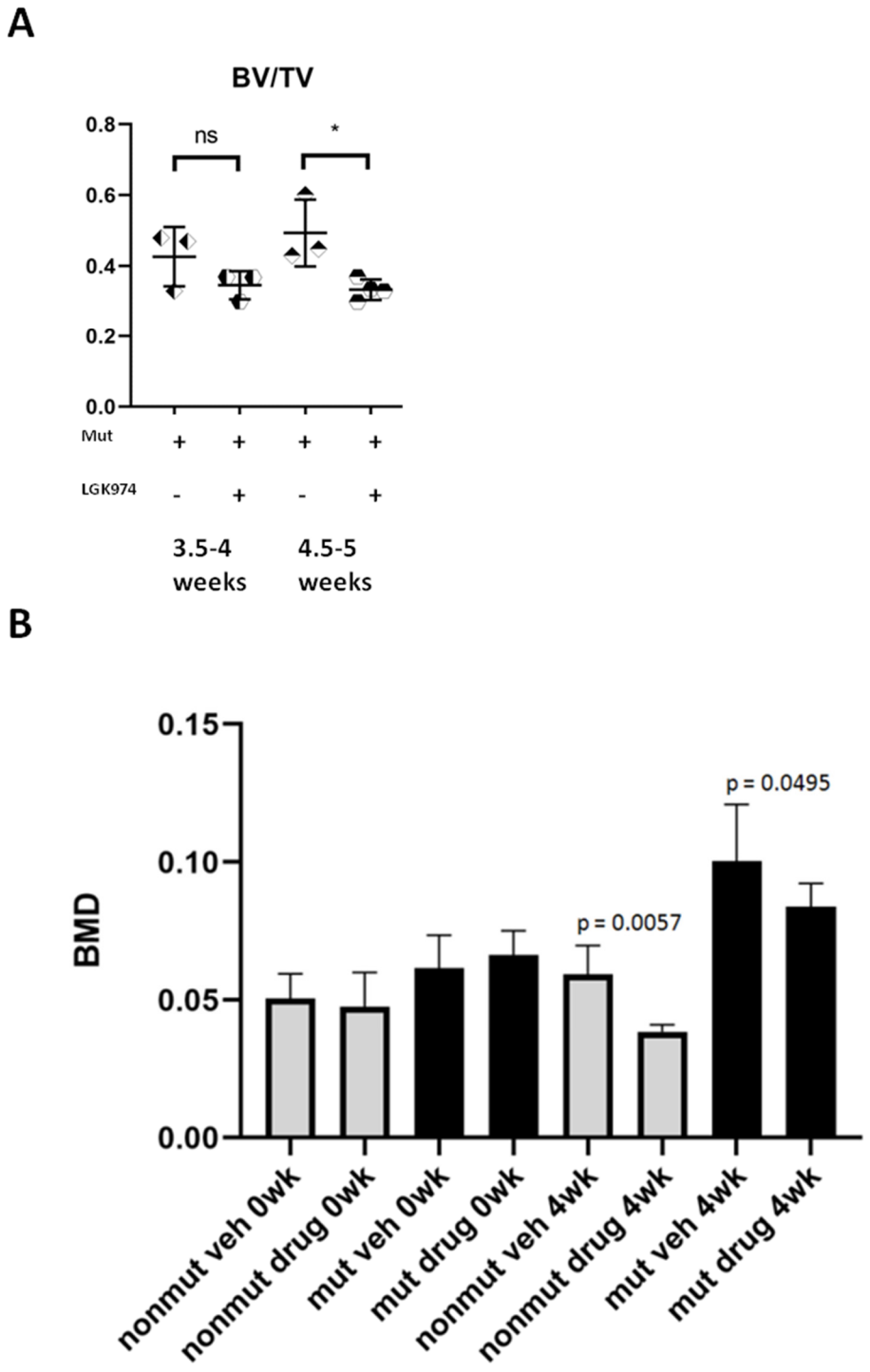


**Figure 2.4.2. Bone densitometry analysis by DEXA shows decreased BMD in high-dose drug-treated group.**

**(A)** CT analyses of mice subgrouped as 3.5-4 (p=0.2071) or 4.5-5 (p=0.0219) weeks of drug.*: p<0.05, ns: not significant.

**(B)** DEXA shows BMD changes at baseline and after 4 weeks of LGK974.

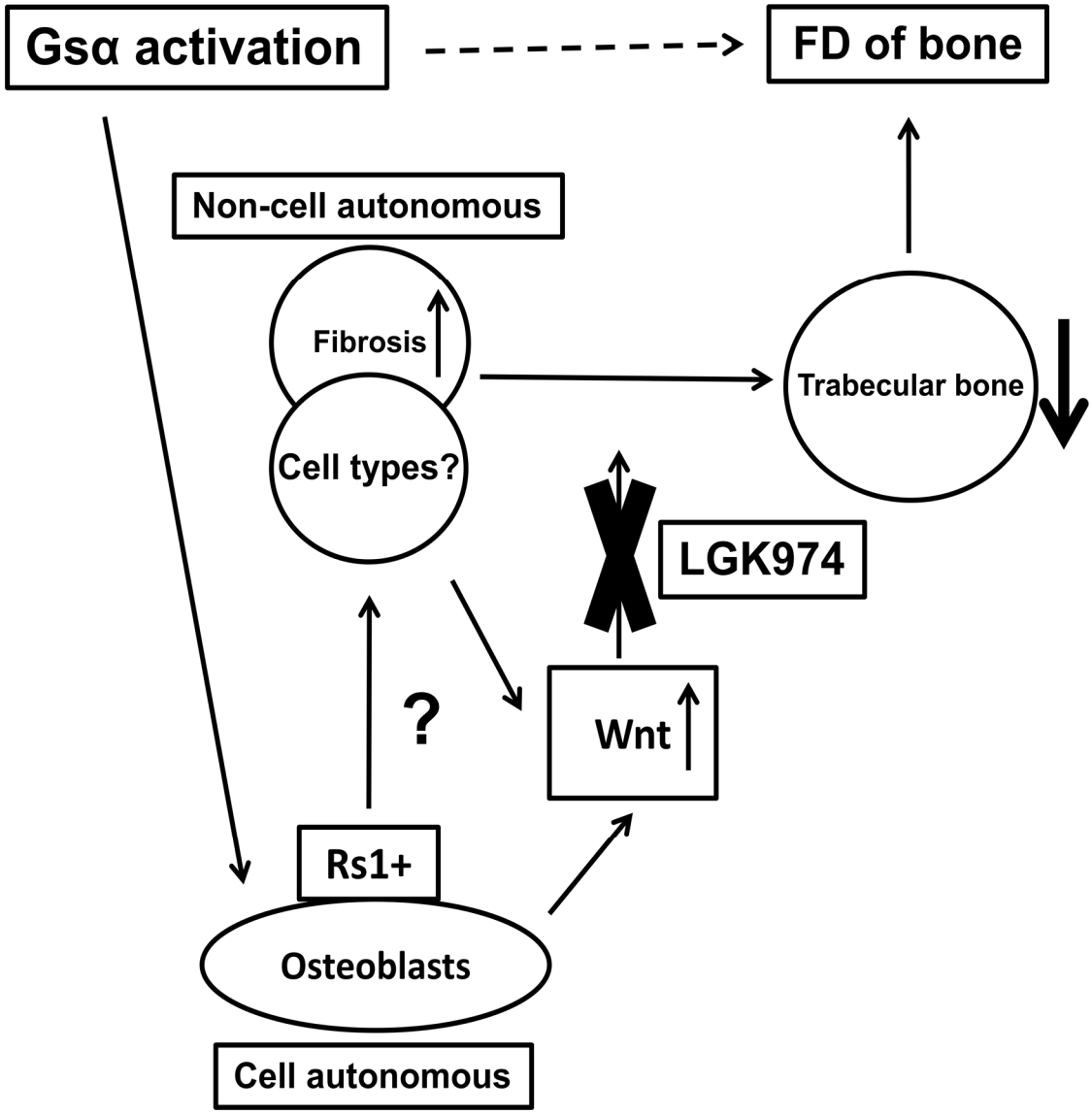


**Figure 2.5. Wnt signaling interactions with Gnas signaling in the Coll(2.3)$^{+}$/Rs1$^{+}$ mouse model of fibrous dysplasia leads to decreased established fibrous dysplastic trabecular bone.**

A working model of the interaction of Wnt signaling and $G_s\alpha$ pathways. Wnt inhibition using LGK974 can lead to decreased pre-existing fibrous dysplastic bone. From our scRNAseq data, both cell autonomous and non-cell autonomous effects are present. Parts of the FD phenotype are still present after the blocking of Wnt signaling, suggesting that non-Wnt pathways remain a major driver of FD lesion formation.

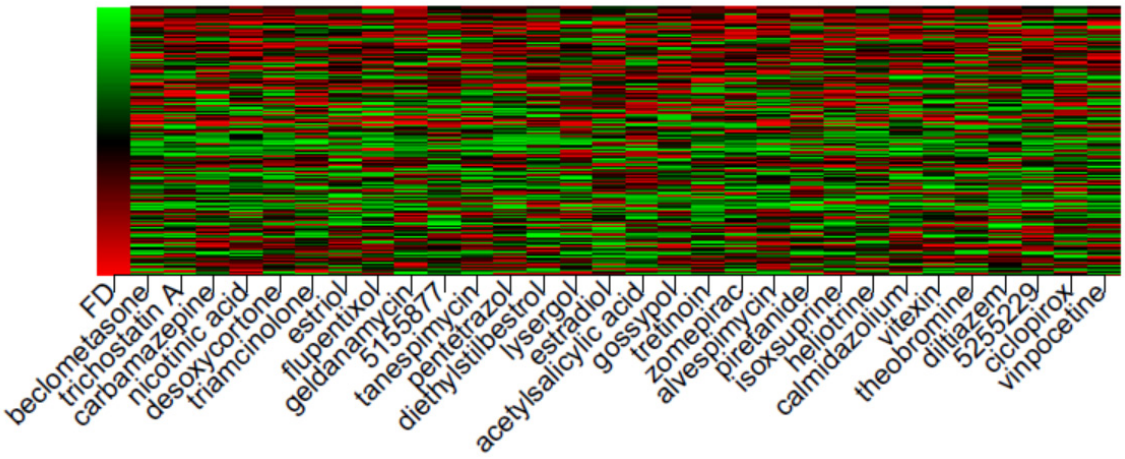


**Figure 3. Drug heatmap from Connectivity Map.**

Drugs that have opposite gene expression to FD were identified for testing of the ability to reverse fibrous dysplasia of the bone. The FD gene expression signature is shown on the left. Drug candidates were from various categories were screened, looking for drug signatures that were opposite of the FD disease signature (e.g., more red on top and more green on the bottom). Potential hit candidates are shown here.

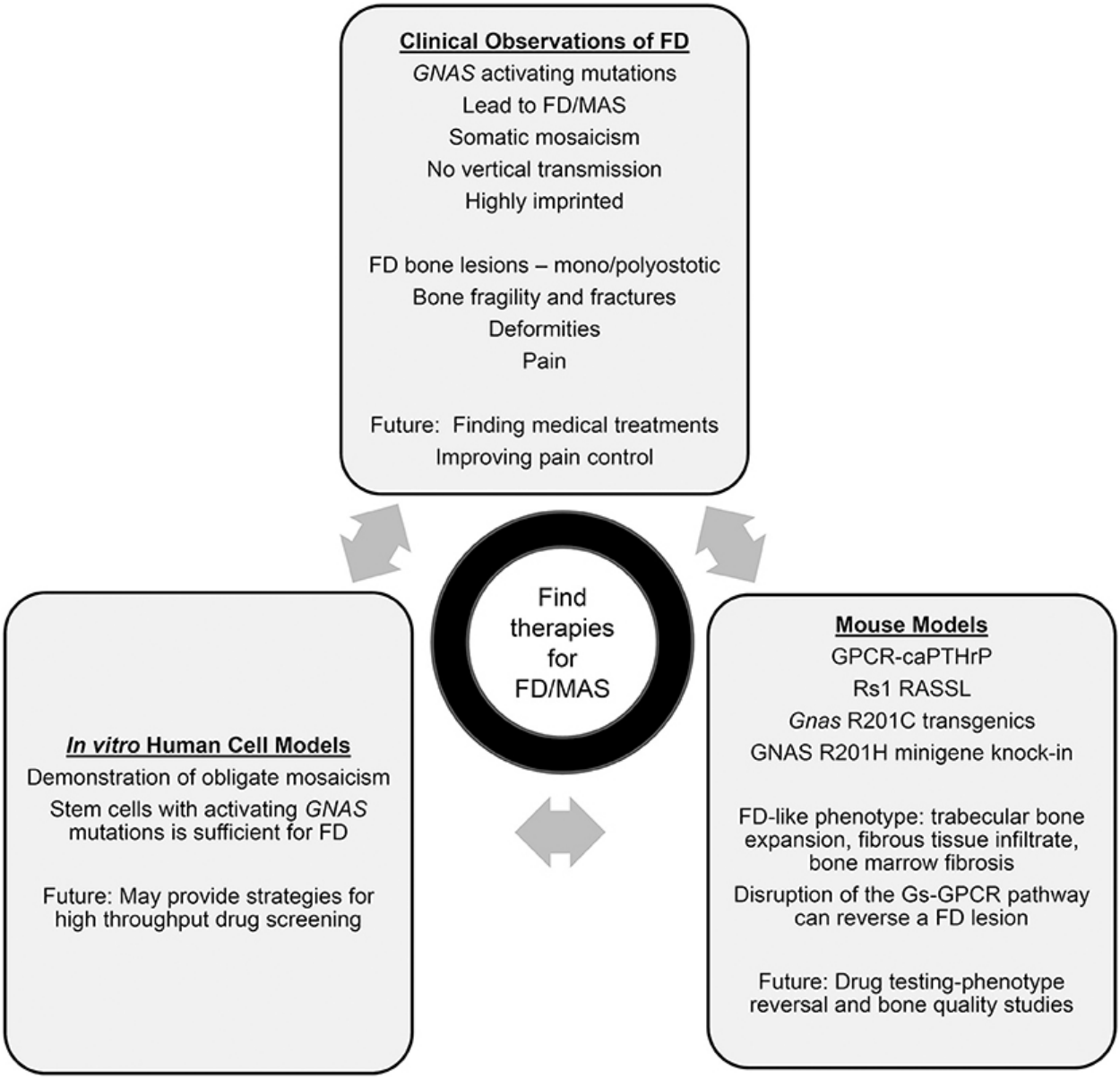


**Figure 4. Summary of human, mouse, and clinical findings in FD.**

## TABLES

### Table 2.1. Dataset filtering and QC steps.

Shows the filtering steps, and the number of cells that were filtered out, as well as the number of remaining cells after each filtering step. The remaining cells in each sample were 2070 to 3562. These procedures were done in Seurat.

WT: wildtype; Mut: Col$I(2.3)^{+}$/$Rs1^{+}$;

(WT1: OB548, WT2: OB776, mut1: OB549, mut2: OB774)

| Dataset Filtering and QC Steps | | | | | | | | | |
|---|---|---|---|---|---|---|---|---|---|
| | | WT1 | | WT2 | | Mut1 | | Mut2 | |
| | | # of Cells Removed | # of Cells Remaining | # of Cells Removed | # of Cells Remaining | # of Cells Removed | # of Cells Remaining | # of Cells Removed | # of Cells Remaining |
| 1 | Number of cells in cellranger filtered output: | | 7974 | | 6874 | | 7463 | | 6484 |
| 2 | Remove background mRNA with SoupX R package. | 0 | 7974 | 0 | 6874 | 0 | 7463 | 0 | 6484 |
| 3 | Remove cells with fewer than 200 genes and remove genes expressed in fewer than 3 cells. | 1840 | 6134 | 1313 | 5561 | 1018 | 6445 | 1100 | 5384 |
| 4 | Remove red blood cells by filtering out cells with greater than 100 Hba-a1 gene transcripts. | 2510 | 3624 | 3110 | 2451 | 2694 | 3751 | 3212 | 2172 |
| 5 | Remove low-quality cells by filtering out cells with greater than 5% mitochondrial genes. | 42 | 3582 | 14 | 2437 | 31 | 3720 | 18 | 2154 |
| 6 | Remove probable doublets by filtering out cells with greater than 5500 genes and remove transcriptome size outliers by removing cells with less than 600 genes. | 14 | 3568 | 0 | 2437 | 5 | 3715 | 1 | 2153 |
| 7 | Remove cells identified as 'Erythrocytes' by SingleR. | 127 | **3441** | 111 | **2326** | 153 | **3562** | 83 | **2070** |

**Table 2.2. Cell numbers in each cluster after filtering.**

The number of cells that were captured and analyzed after filtering are as listed (2070 to 3562 cells).The cell numbers and number of differential genes in each cluster (0-10) are also listed These procedures were done in Seurat.

WT: wildtype; Mut: ColI(2.3)$^{+}$/Rs1$^{+}$;

(WT1: OB548, WT2: OB776, Mut1: OB549, Mut2: OB774)

| Cell numbers in each cluster | | | | | | | | | | | | | | | | |
|---|---|---|---|---|---|---|---|---|---|---|---|---|---|---|---|---|
| | Estimated number of cells | Mean reads per cell | Median genes per cell | Cell numbers in each cluster (after filtering) | | | | | | | | | | | | |
| | | | | Cluster | 0 | 1 | 2 | 3 | 4 | 5 | 6 | 7 | 8 | 9 | 10 | Total |
| WT1 | **7974** | 67922 | 856 | WT1 | 798 | 484 | 506 | 450 | 290 | 330 | 294 | 117 | 48 | 99 | 25 | 3441 |
| WT2 | **6874** | 56569 | 803 | WT2 | 534 | 264 | 297 | 189 | 366 | 189 | 198 | 196 | 9 | 57 | 27 | 2326 |
| Total number of cells in WT | 14848 | | | Total number of cells in WT | 1332 | 748 | 803 | 639 | 656 | 519 | 492 | 313 | 57 | 156 | 52 | **5767** |
| | | | | Percentage (%) of WT | 23.1 | 12.97 | 13.92 | 11.08 | 11.37 | 9 | 8.53 | 5.43 | 0.99 | 2.71 | 0.9 | 100 |
| Mut1 | **7463** | 49934 | 1037 | Mut1 | 589 | 643 | 466 | 469 | 244 | 382 | 279 | 118 | 265 | 84 | 23 | 3562 |
| Mut2 | **6484** | 84283 | 798 | Mut2 | 522 | 266 | 321 | 221 | 212 | 129 | 112 | 128 | 94 | 47 | 18 | 2070 |
| Total number of cells in Mut | 13947 | | | Total number of cells in Mut | 1111 | 909 | 787 | 690 | 456 | 511 | 391 | 246 | 359 | 131 | 41 | **5632** |
| | | | | Percentage (%) of Mut | 19.73 | 16.14 | 13.97 | 12.25 | 8.1 | 9.07 | 6.94 | 4.37 | 6.37 | 2.33 | 0.73 | 100 |
| Total of WT and Mut | **28795** | | | Total number of cells in each Cluster | 2443 | 1657 | 1590 | 1329 | 1112 | 1030 | 883 | 559 | 416 | 287 | 93 | **11399** |
| | | | | Number of differential expression genes in each cluster | | | | | | | | | | | | |
| | | | | Cluster | 0 | 1 | 2 | 3 | 4 | 5 | 6 | 7 | 8 | 9 | 10 | Total |
| | | | | No. of Genes | 16 | 6 | 8 | 54 | 40 | 20 | 19 | 47 | 903 | 96 | 337 | 1546 |

**Table 2.3. Cell numbers in SingleR cell type prediction.**

The number of cells from each cluster in each cell type predicted by SingleR are listed.

| Cluster | 0 | 1 | 2 | 3 | 4 | 5 | 6 | 7 | 8 | 9 | 10 |
|---|---|---|---|---|---|---|---|---|---|---|---|
| SingleR cell type | | | | | | | | | | | |
| B cells | 0 | 0 | 1 | 2 | 969 | 13 | 240 | 0 | 0 | 4 | 1 |
| Dendritic cells | 0 | 0 | 0 | 0 | 0 | 0 | 1 | 0 | 0 | 8 | 5 |
| Endothelial cells | 0 | 0 | 0 | 0 | 0 | 0 | 0 | 0 | 15 | 0 | 0 |
| Fibroblasts | 0 | 0 | 0 | 0 | 0 | 0 | 2 | 0 | 390 | 0 | 0 |
| Granulocytes | 2440 | 1653 | 1589 | 1317 | 141 | 256 | 54 | 21 | 5 | 30 | 40 |
| Macrophages | 0 | 0 | 0 | 0 | 0 | 2 | 1 | 1 | 3 | 0 | 0 |
| Monocytes | 2 | 2 | 0 | 9 | 2 | 757 | 440 | 537 | 3 | 0 | 44 |
| NK cells | 0 | 0 | 0 | 1 | 0 | 0 | 44 | 0 | 0 | 169 | 2 |
| T cells | 1 | 2 | 0 | 0 | 0 | 2 | 101 | 0 | 0 | 76 | 1 |

**Table 3. Candidate drugs from drug repositioning.**

Potential drugs for treatment of FD from the drug repositioning pipeline showed drugs in various categories.

| Drug name | Category (target) |
|---|---|
| Geldanamycin | HSP90 |
| Estriol | Hormone |
| Acetylsalicylic Acid | NSAID |
| Nicotinic Acid | GPCR |
| Gossypol | GPCR |
| Trichostatin A | Miscellaneous Anti-fungal |
| Desoxycortone | Steroid |
| Triamcinolone | Steroid |
| Carbamazepine | Ion channel |

## REFERENCES


1. Fredriksson, R., et al., *The G-protein-coupled receptors in the human genome form five main families. Phylogenetic analysis, paralogon groups, and fingerprints.* Mol Pharmacol, 2003. **63**(6): p. 1256-72.
2. Brink, C.B., et al., *Recent advances in drug action and therapeutics: relevance of novel concepts in G-protein-coupled receptor and signal transduction pharmacology.* Br J Clin Pharmacol, 2004. **57**(4): p. 373-87.
3. Gether, U., *Uncovering molecular mechanisms involved in activation of G protein-coupled receptors.* Endocr Rev, 2000. **21**(1): p. 90-113.
4. Chapurlat, R.D. and P. Orcel, *Fibrous dysplasia of bone and McCune-Albright syndrome.* Best practice & research. Clinical rheumatology, 2008. **22**(1): p. 55-69.
5. Chapurlat, R.D., et al., *Pathophysiology and medical treatment of pain in fibrous dysplasia of bone.* Orphanet J Rare Dis, 2012. **7 Suppl 1**: p. S3.
6. Javaid, M.K., et al., *Best practice management guidelines for fibrous dysplasia/McCune-Albright syndrome: a consensus statement from the FD/MAS international consortium.* Orphanet J Rare Dis, 2019. **14**(1): p. 139.
7. Boyce, A.M., et al., *Denosumab treatment for fibrous dysplasia.* J Bone Miner Res, 2012. **27**(7): p. 1462-70.
8. Florenzano, P., et al., *Age-Related Changes and Effects of Bisphosphonates on Bone Turnover and Disease Progression in Fibrous Dysplasia of Bone.* J Bone Miner Res, 2019. **34**(4): p. 653-660.
9. Majoor, B.C., et al., *Outcome of Long-Term Bisphosphonate Therapy in McCune-Albright Syndrome and Polyostotic Fibrous Dysplasia.* J Bone Miner Res, 2017. **32**(2): p. 264-276.
10. Boyce, A.M., et al., *A randomized, double blind, placebo-controlled trial of alendronate treatment for fibrous dysplasia of bone.* J Clin Endocrinol Metab, 2014. **99**(11): p. 4133-40.
11. Calvi, L.M., et al., *Activated parathyroid hormone/parathyroid hormone-related protein receptor in osteoblastic cells differentially affects cortical and trabecular bone.* J Clin Invest, 2001. **107**(3): p. 277-86.
12. Kuznetsov, S.A., et al., *The interplay of osteogenesis and hematopoiesis: expression of a constitutively active PTH/PTHrP receptor in osteogenic cells perturbs the establishment*

*of hematopoiesis in bone and of skeletal stem cells in the bone marrow.* J Cell Biol, 2004. **167**(6): p. 1113-22.

13. Conklin, B.R., et al., *Engineering GPCR signaling pathways with RASSLs.* Nat Methods, 2008. **5**(8): p. 673-8.
14. Chang, W.C., et al., *Modifying ligand-induced and constitutive signaling of the human 5-HT4 receptor.* PLoS One, 2007. **2**(12): p. e1317.
15. Hsiao, E.C., et al., *Gs G protein-coupled receptor signaling in osteoblasts elicits age-dependent effects on bone formation.* J Bone Miner Res, 2010. **25**(3): p. 584-93.
16. Kazakia, G.J., et al., *Mineral composition is altered by osteoblast expression of an engineered G(s)-coupled receptor.* Calcif Tissue Int, 2011. **89**(1): p. 10-20.
17. Schepers, K., et al., *Activated Gs signaling in osteoblastic cells alters the hematopoietic stem cell niche in mice.* Blood, 2012. **120**(17): p. 3425-35.
18. Cain, C.J., et al., *Increased Gs Signaling in Osteoblasts Reduces Bone Marrow and Whole-Body Adiposity in Male Mice.* Endocrinology, 2016. **157**(4): p. 1481-94.
19. Saggio, I., et al., *Constitutive expression of Gsalpha(R201C) in mice produces a heritable, direct replica of human fibrous dysplasia bone pathology and demonstrates its natural history.* J Bone Miner Res, 2014. **29**(11): p. 2357-68.
20. Remoli, C., et al., *Osteoblast-specific expression of the fibrous dysplasia (FD)-causing mutation Gsalpha(R201C) produces a high bone mass phenotype but does not reproduce FD in the mouse.* J Bone Miner Res, 2015. **30**(6): p. 1030-43.
21. Hsiao, E.C., et al., *Osteoblast expression of an engineered Gs-coupled receptor dramatically increases bone mass.* Proc Natl Acad Sci U S A, 2008. **105**(4): p. 1209-14.
22. Palmisano, B., et al., *RANKL Inhibition in Fibrous Dysplasia of Bone: A Preclinical Study in a Mouse Model of the Human Disease.* J Bone Miner Res, 2019. **34**(12): p. 2171-2182.
23. Zhao, X., et al., *Expression of an active Galphas mutant in skeletal stem cells is sufficient and necessary for fibrous dysplasia initiation and maintenance.* Proc Natl Acad Sci U S A, 2018. **115**(3): p. E428-E437.
24. Khan, S.K., et al., *Induced Gnas(R201H) expression from the endogenous Gnas locus causes fibrous dysplasia by up-regulating Wnt/beta-catenin signaling.* Proc Natl Acad Sci U S A, 2018. **115**(3): p. E418-E427.
25. Xu, R., et al., *Galphas signaling controls intramembranous ossification during cranial bone development by regulating both Hedgehog and Wnt/beta-catenin signaling.* Bone Res, 2018. **6**: p. 33.
26. Bianco, P., et al., *Reproduction of human fibrous dysplasia of bone in immunocompromised mice by transplanted mosaics of normal and Gsalpha-mutated skeletal progenitor cells.* J Clin Invest, 1998. **101**(8): p. 1737-44.

27. Kuznetsov, S.A., et al., *Age-dependent demise of GNAS-mutated skeletal stem cells and "normalization" of fibrous dysplasia of bone.* J Bone Miner Res, 2008. **23**(11): p. 1731-40.
28. Piersanti, S., et al., *Transfer, analysis, and reversion of the fibrous dysplasia cellular phenotype in human skeletal progenitors.* J Bone Miner Res, 2010. **25**(5): p. 1103-16.
29. de Castro, L.F., et al., *Activation of RANK/RANKL/OPG Pathway Is Involved in the Pathophysiology of Fibrous Dysplasia and Associated With Disease Burden.* J Bone Miner Res, 2019. **34**(2): p. 290-294.
30. Wu, J.Y., D.T. Scadden, and H.M. Kronenberg, *Role of the osteoblast lineage in the bone marrow hematopoietic niches.* J Bone Miner Res, 2009. **24**(5): p. 759-64.
31. Calvi, L.M., et al., *Osteoblastic cells regulate the haematopoietic stem cell niche.* Nature, 2003. **425**(6960): p. 841-6.
32. Wang, L., et al., *Loss of Gi G-Protein-Coupled Receptor Signaling in Osteoblasts Accelerates Bone Fracture Healing.* J Bone Miner Res, 2015. **30**(10): p. 1896-904.
33. Alkhiary, Y.M., et al., *Enhancement of experimental fracture-healing by systemic administration of recombinant human parathyroid hormone (PTH 1-34).* J Bone Joint Surg Am, 2005. **87**(4): p. 731-41.
34. Jilka, R.L., *Molecular and cellular mechanisms of the anabolic effect of intermittent PTH.* Bone, 2007. **40**(6): p. 1434-46.
35. van der Horst, G., et al., *Multiple mechanisms are involved in inhibition of osteoblast differentiation by PTHrP and PTH in KS483 Cells.* J Bone Miner Res, 2005. **20**(12): p. 2233-44.
36. Regard, J.B., et al., *Wnt signaling in bone development and disease: making stronger bone with Wnts.* Cold Spring Harb Perspect Biol, 2012. **4**(12).
37. Pan, A., et al., *A review of hedgehog signaling in cranial bone development.* Frontiers in physiology, 2013. **4**: p. 61.
38. Yu, F.X., et al., *Regulation of the Hippo-YAP pathway by G-protein-coupled receptor signaling.* Cell, 2012. **150**(4): p. 780-91.
39. Moon, R.T., et al., *The promise and perils of Wnt signaling through β-catenin.* Science, 2002. **296**(5573): p. 1644-1646.
40. Liang, W.-C., et al., *H19 activates Wnt signaling and promotes osteoblast differentiation by functioning as a competing endogenous RNA.* Scientific reports, 2016. **6**: p. 20121.
41. Cawthorn, W.P., et al., *Wnt6, Wnt10a and Wnt10b inhibit adipogenesis and stimulate osteoblastogenesis through a beta-catenin-dependent mechanism.* Bone, 2012. **50**(2): p. 477-89.

42. Regard, J.B., et al., *Wnt/beta-catenin signaling is differentially regulated by Galpha proteins and contributes to fibrous dysplasia.* Proc Natl Acad Sci U S A, 2011. **108**(50): p. 20101-6.
43. Cheng, F., et al., *Prediction of drug-target interactions and drug repositioning via network-based inference.* PLoS Comput Biol, 2012. **8**(5): p. e1002503.
44. Csermely, P., et al., *Structure and dynamics of molecular networks: a novel paradigm of drug discovery: a comprehensive review.* Pharmacology & therapeutics, 2013. **138**(3): p. 333-408.
45. Houschyar, K.S., et al., *Wnt signaling induces epithelial differentiation during cutaneous wound healing.* Organogenesis, 2015. **11**(3): p. 95-104.
46. Clevers, H., *Wnt/β-catenin signaling in development and disease.* Cell, 2006. **127**(3): p. 469-480.
47. Chen, C., et al., *Aberrant activation of Wnt/β-catenin signaling drives proliferation of bone sarcoma cells.* Oncotarget, 2015. **6**(19): p. 17570.
48. Thrasivoulou, C., M. Millar, and A. Ahmed, *Activation of intracellular calcium by multiple Wnt ligands and translocation of β-catenin into the nucleus a convergent model of wnt/ca2+ and wnt/β-catenin pathways.* Journal of Biological Chemistry, 2013. **288**(50): p. 35651-35659.
49. Herr, P. and K. Basler, *Porcupine-mediated lipidation is required for Wnt recognition by Wls.* Developmental biology, 2012. **361**(2): p. 392-402.
50. Young, M.D. and S. Behjati, *SoupX removes ambient RNA contamination from droplet based single cell RNA sequencing data.* BioRxiv, 2020: p. 303727.
51. Butler, A., et al., *Integrating single-cell transcriptomic data across different conditions, technologies, and species.* Nature biotechnology, 2018. **36**(5): p. 411-420.
52. Stuart, T., et al., *Comprehensive integration of single-cell data.* Cell, 2019. **177**(7): p. 1888-1902. e21.
53. Aran, D., et al., *Reference-based analysis of lung single-cell sequencing reveals a transitional profibrotic macrophage.* Nat Immunol, 2019. **20**(2): p. 163-172.
54. Han, X., et al., *Mapping the mouse cell atlas by microwell-seq.* Cell, 2018. **172**(5): p. 1091-1107. e17.
55. Kuleshov, M.V., et al., *Enrichr: a comprehensive gene set enrichment analysis web server 2016 update.* Nucleic acids research, 2016. **44**(W1): p. W90-7.
56. Krämer, A., et al., *Causal analysis approaches in ingenuity pathway analysis.* Bioinformatics, 2014. **30**(4): p. 523-530.
57. Trapnell, C., et al., *The dynamics and regulators of cell fate decisions are revealed by pseudotemporal ordering of single cells.* Nat Biotechnol, 2014. **32**(4): p. 381-386.

58. Djomehri, S.I., et al., *Mineral density volume gradients in normal and diseased human tissues.* PLoS One, 2015. **10**(4): p. e0121611.
59. Liang, K.-Y. and S.L. Zeger, *Longitudinal data analysis using generalized linear models.* Biometrika, 1986. **73**(1): p. 13-22.
60. Riminucci, M., et al., *The histopathology of fibrous dysplasia of bone in patients with activating mutations of the Gs alpha gene: site-specific patterns and recurrent histological hallmarks.* J Pathol, 1999. **187**(2): p. 249-58.
61. Butler, A., et al., *Integrating single-cell transcriptomic data across different conditions, technologies, and species.* Nat Biotechnol, 2018. **36**(5): p. 411-420.
62. Stuart, T., et al., *Comprehensive Integration of Single-Cell Data.* Cell, 2019. **177**(7): p. 1888-1902 e21.
63. Bi, W., et al., *Sox9 is required for cartilage formation.* Nature genetics, 1999. **22**(1): p. 85-89.
64. Majoor, B.C., et al., *Increased Risk of Breast Cancer at a Young Age in Women with Fibrous Dysplasia.* J Bone Miner Res, 2018. **33**(1): p. 84-90.
65. Wattanachanya, L., et al., *Assessing the osteoblast transcriptome in a model of enhanced bone formation due to constitutive Gs-G protein signaling in osteoblasts.* Exp Cell Res, 2015. **333**(2): p. 289-302.
66. Tang, Q.Q. and M.D. Lane, *Adipogenesis: from stem cell to adipocyte.* Annu Rev Biochem, 2012. **81**: p. 715-36.
67. Liu, J., et al., *Targeting Wnt-driven cancer through the inhibition of Porcupine by LGK974.* Proc Natl Acad Sci U S A, 2013. **110**(50): p. 20224-9.
68. Madan, B., et al., *Bone loss from Wnt inhibition mitigated by concurrent alendronate therapy.* Bone Research, 2018. **6**(1): p. 17.
69. Juppner, H., et al., *A G protein-linked receptor for parathyroid hormone and parathyroid hormone-related peptide.* Science, 1991. **254**(5034): p. 1024-6.
70. Kasperk, C.H., et al., *Endothelin-1 is a potent regulator of human bone cell metabolism in vitro.* Calcif Tissue Int, 1997. **60**(4): p. 368-74.
71. Suzawa, T., et al., *The role of prostaglandin E receptor subtypes (EP1, EP2, EP3, and EP4) in bone resorption: an analysis using specific agonists for the respective EPs.* Endocrinology, 2000. **141**(4): p. 1554-9.
72. Moore, R.E., et al., *Characterization of beta-adrenergic receptors on rat and human osteoblast-like cells and demonstration that beta-receptor agonists can stimulate bone resorption in organ culture.* Bone Miner, 1993. **23**(3): p. 301-15.

73. Togari, A., et al., *Expression of mRNAs for neuropeptide receptors and beta-adrenergic receptors in human osteoblasts and human osteogenic sarcoma cells.* Neurosci Lett, 1997. **233**(2-3): p. 125-8.
74. Abe, E., et al., *TSH is a negative regulator of skeletal remodeling.* Cell, 2003. **115**(2): p. 151-62.
75. Vilarino-Guell, C., et al., *PTHR1 Polymorphisms Influence BMD Variation through Effects on the Growing Skeleton.* Calcif Tissue Int, 2007.
76. Kotelnikova, E., et al., *Novel approach to meta-analysis of microarray datasets reveals muscle remodeling-related drug targets and biomarkers in Duchenne muscular dystrophy.* PLoS Comput Biol, 2012. **8**(2): p. e1002365.
77. Chen, R., et al., *A meta-analysis of lung cancer gene expression identifies PTK7 as a survival gene in lung adenocarcinoma.* Cancer research, 2014. **74**(10): p. 2892-2902.
78. McIntyre, R.S., et al., *Advancing biomarker research: utilizing 'Big Data'approaches for the characterization and prevention of bipolar disorder.* Bipolar disorders, 2014. **16**(5): p. 531-547.
79. Lamb, J., et al., *The Connectivity Map: using gene-expression signatures to connect small molecules, genes, and disease.* science, 2006. **313**(5795): p. 1929-1935.
80. Duan, Q., et al., *LINCS Canvas Browser: interactive web app to query, browse and interrogate LINCS L1000 gene expression signatures.* Nucleic acids research, 2014. **42**(W1): p. W449-W460.
81. Subramanian, A., et al., *A Next Generation Connectivity Map: L1000 Platform and the First 1,000,000 Profiles.* Cell, 2017. **171**(6): p. 1437-1452 e17.
82. Sirota, M., et al., *Discovery and preclinical validation of drug indications using compendia of public gene expression data.* Sci Transl Med, 2011. **3**(96): p. 96ra77.
83. Dudley, J.T., et al., *Computational repositioning of the anticonvulsant topiramate for inflammatory bowel disease.* Sci Transl Med, 2011. **3**(96): p. 96ra76.
84. Wattanachanya, L., et al., *Assessing the osteoblast transcriptome in a model of enhanced bone formation due to constitutive G-G protein signaling in osteoblasts.* Experimental cell research, 2015.
85. Chen, B., et al., *Reversal of cancer gene expression correlates with drug efficacy and reveals therapeutic targets.* Nat Commun, 2017. **8**: p. 16022.
86. Chen, B., et al., *Computational Discovery of Niclosamide Ethanolamine, a Repurposed Drug Candidate That Reduces Growth of Hepatocellular Carcinoma Cells In Vitro and in Mice by Inhibiting Cell Division Cycle 37 Signaling.* Gastroenterology, 2017. **152**(8): p. 2022-2036.

87. Lung, H., E.C. Hsiao, and K.L. Wentworth, *Advances in Models of Fibrous Dysplasia/McCune-Albright Syndrome.* Front Endocrinol (Lausanne), 2019. **10**: p. 925.
88. Bianco, P., et al., *Mutations of the GNAS1 gene, stromal cell dysfunction, and osteomalacic changes in non-McCune-Albright fibrous dysplasia of bone.* J Bone Miner Res, 2000. **15**(1): p. 120-8.

**Publishing Agreement**

It is the policy of the University to encourage open access and broad distribution of all theses, dissertations, and manuscripts. The Graduate Division will facilitate the distribution of UCSF theses, dissertations, and manuscripts to the UCSF Library for open access and distribution. UCSF will make such theses, dissertations, and manuscripts accessible to the public and will take reasonable steps to preserve these works in perpetuity.

I hereby grant the non-exclusive, perpetual right to The Regents of the University of California to reproduce, publicly display, distribute, preserve, and publish copies of my thesis, dissertation, or manuscript in any form or media, now existing or later derived, including access online for teaching, research, and public service purposes.

DocuSigned by:
Hsuan Lung
CF64E35C665D4AE...
Author Signature

12/18/2020
Date